Chemical Engineering Journal 485 (2024) 149787

Contents lists available at ScienceDirect

Chemical Engineering Journal

journal homepage: www.elsevier.com/locate/cej

Synergistic enhancement of CO_2 hydrogenation to C_{5+} hydrocarbons using mixed Fe_5C_2 and Na-Fe_3O_4 catalysts: Effects of oxide/carbide ratio, proximity, and reduction

Sara Najari [a,*], Samrand Saeidi [b,*], András Sápi [a,*], Ákos Szamosvölgyi [a], Ádám Papp [a], Anastasiia Efremova [a], Henrik Bali [a], Zoltán Kónya [a,c]

[a] Department of Applied and Environmental Chemistry, Interdisciplinary Excellence Centre, University of Szeged, Rerrich Béla tér 1, Szeged 6720, Hungary
[b] Department of Technologies and Installations for Waste Management, Faculty of Energy and Environmental Engineering, Silesian University of Technology, Konarskiego 18, 44-100 Gliwice, Poland
[c] HUN-REN-SZTE Reaction Kinetics and Surface Chemistry Research Group, Rerrich Béla tér 1, Szeged 6720, Hungary

ARTICLE INFO

Keywords:
CO_2 hydrogenation
Iron oxide/iron carbide ratio
Proximity
Reduction
Synergistic effect
C_{5+} hydrocarbons

ABSTRACT

CO_2 hydrogenation into sustainable chemical feedstocks and fuels is a pivotal focus of energy research. Fe-based catalysts have emerged as promising candidates due to their high efficiency in the CO_2 hydrogenation toward C_2–C_4 olefins and C_{5+} hydrocarbons. Fe_5C_2 is known as the active phase of the CO_2 hydrogenation. Therefore, it is imperative to discern the roles of active phases in product distribution. Accordingly, in the present study, Fe_5C_2 is synthesized separately and physically mixed with Na-Fe_3O_4. The effects of oxide/carbide ratio, the proximity of active phases, and reduction treatment are investigated. The results show that adding carbide to oxide in an appropriate ratio significantly increases CO_2 conversion due to the controlled reduction of the oxide phase and enhanced CO_2 adsorption. Additionally, a closer distance (mixed-powder pellets) between Na-Fe_3O_4 and Fe_5C_2 results in higher selectivity for C_2-C_4 olefins and C_{5+} hydrocarbons and less CH_4. Furthermore, the graphitized layers of reduced catalyst (R-Na-Fe_3O_4/Fe_5C_2 (70/30 wt%)) enhance the selectivity to C_2-C_4 olefins (40 %) and C_{5+} hydrocarbons (35 %) at around 40 % CO_2 conversion. In contrast, amorphous carbon in the non-reduced catalyst (NR-Na-Fe_3O_4/Fe_5C_2 (70/30 wt%)) favors more C_2-C_4 paraffins and CH_4. Therefore, the interplay between the influential factors, i.e., oxide/carbide ratio, spatial distance, and reduction treatment, can result in tailoring an efficient CO_2 hydrogenation catalyst toward the formation of valuable hydrocarbons.

1. Introduction

CO_2 hydrogenation is regarded as a promising process for the production of valuable chemicals and fuels via reverse water gas shift (RWGS) and Fischer-Tropsch synthesis (FTS) while also helping mitigate anthropogenic CO_2 emissions [1,2]. Optimizing CO_2 hydrogenation for value-added product involves three crucial factors: operating conditions [3,4], reactor configuration [5,6], and catalyst type [7,8]. The impact of catalyst type on enhancing the performance of the CO_2 hydrogenation process is undeniable. Iron-based catalysts are favored among potential catalysts due to their high activity, low cost, and the olefinic nature of the products they yield. Iron catalysts form Hägg carbide (χ-Fe_5C_2) in-situ as the active phase during CO_2 hydrogenation [9,10]. It is generally accepted that the iron carbides serve as the active phase during the FTS reaction [11–13]. In recent years, researchers have focused on enhancing the performance of iron-based catalysts and investigating the relationship between iron carbide phases and catalytic performance in FTS reactions [14,15].

Typically, iron catalysts need alkali metal promotion to attain the desired activity and selectivity. The addition of sodium (Na) has been reported to be beneficial for olefin production [16,17]. The presence of Na obviously enhances the surface basicity and carburization of iron-based catalysts, making them highly active for CO_2 hydrogenation into light olefins [18,19].

Despite the existing research reports, the precise role of the iron oxide component in Fe-based catalysts in CO_2 hydrogenation still needs to be better understood [20]. Iron carbides undergo phase changes during the FTS, leading to low catalytic performance [21]. Extensive

* Corresponding authors.
E-mail addresses: sara.najari@chem.u-szeged.hu (S. Najari), samrand.saeidi@polsl.pl (S. Saeidi), sapia@chem.u-szeged.hu (A. Sápi).

https://doi.org/10.1016/j.cej.2024.149787

Available online 17 February 2024

research has been devoted to developing core–shell catalysts using a protective layer to enhance the stability of iron carbides [22,23]. Among these catalysts, those derived from metal-organic frameworks (MOF), known as metal@C, have been extensively explored. However, the effectiveness of the carbon shell in these catalysts is limited, as it can hinder the interaction between gas molecules and the active phases [24].

Defects in carbon materials have been suggested to offer several beneficial effects in catalytic processes. These defects facilitate the mass transfer of reactants, provide anchoring sites for metal nanoparticles, and serve as active sites for catalytic reactions. In graphite, carbon defects have been identified as active sites for acidic oxygen reduction reactions. Additionally, defects in graphene layers are crucial in enhancing FTS performance [25,26].

In defect-rich graphene-supported iron catalysts, a tunable interaction between the metal and the support is achieved, with defects serving as favorable nucleation sites for anchoring iron nanoparticles. While it is evident that carbon defects play significant roles in FTS reactions with iron-based catalysts, the precise and unambiguous correlation between carbon defects and FTS performance remains a topic that still needs to be fully understood [27]. Moreover, the synergistic effect between iron oxide and iron carbide, which enhances alkene formation in CO_2 hydrogenation, has remained unclear [28,29]. Nevertheless, there has been limited research exploring the influence of carbon materials in conjunction with iron oxide for CO_2 hydrogenation.

The evolution process of transforming iron catalyst precursors into FTS catalysts through thermal treatment is intricate and dynamic. Our understanding of its function during CO_2 hydrogenation remains unclear due to various factors, including unique preparation methods, initial oxide/carbide ratio, the presence of promoters, variations in reduction conditions, and the proximity of active sites [30]. These complexities contribute to the ongoing debate surrounding the nature of the active phase in CO_2-FTS reaction over Fe-based catalysts, making it controversial. Therefore, it is crucial to design an appropriate catalytic system to gain deeper insights into the role of iron carbides in the catalytic activity of this reaction [31]. Furthermore, it is essential to highlight that the carburization process is influenced by the intricate surface microenvironment, where competitive reactions such as oxygen removal, carbon permeation, hydrogenation, and carbon deposition occur. Yang et al. [32] synthesized Fe_5C_2 and Fe_3C using carburization of Fe-oxalate in a CO environment at different temperatures. Tang et al. [33] successfully manipulated these processes, producing high-purity Fe_5C_2 and establishing it as an efficient FTS catalyst. In addition, Skrypnik et al. [34,35] prepared well-defined $Fe_xO_yC_z$ compositions through controlled decomposition of iron oxalate under an inert atmosphere and different temperatures to elucidate the role of different active Fe-species in CO_2 hydrogenation reactions. They established a relationship between reaction pathways, catalyst performance, and the steady-state composition of the catalyst, which provides an opportunity for catalyst design and preparation.

Lyu et al. [36] produced nanocrystals of ε-Fe_2C encapsulated in graphene layers for the Fischer-Tropsch (FT) reaction. These nanocrystals demonstrated remarkable activity and stability under practical FT synthesis conditions. Graphene layers exerted a confinement effect, stabilizing the metastable yet highly active ε-Fe_2C phase. The distinctive confinement structure (ε-Fe_2C@graphene) effectively prevented the formation of an amorphous carbon layer, thus preserving the catalytically active phase from converting into less carbon-efficient phases.

However, few studies have focused on introducing the iron carbide into the starting material in a physical mixture, although Fe_5C_2 is considered the active phase of FTS in the presence of either a graphitic or amorphous shell. Nonetheless, little attention has been given to fine-tuning the nature of the carbon shell toward a more graphitic and defective carbon structure, which is known to exhibit superior CO_2 hydrogenation performance. Additionally, the impact of operating conditions on the formation of this carbon shell during the reaction has been largely overlooked [37,38].

For instance, Nawaz et al. [39] fabricated highly dispersed Fe_3O_4 nanocrystals on activated carbon (AC) using a sole precipitation method. These nanocrystals are proposed as a promising candidate for enhancing the dually embedded carbide nanocomposites (consisting of χ-Fe_5C_2 and θ-Fe_3C) in the Na-FeCa@AC/HZSM-5 catalyst. The sole precipitation method effectively confined Fe@AC species within the rigid geometry of defective graphite patches, thus mitigating the sintering and agglomeration of Fe nanoparticles. Furthermore, it was shown that the encapsulation of perforated carbon layers during carburization greatly enhanced the stability of the highly active carbide phase while preventing the formation of inactive carbon deposits.

Jin et al. [40] recently synthesized a Fe/C catalyst to convert CO_2 into light olefins directly. The catalyst displayed high selectivity for light olefins (up to 63.0 %) at the CO_2 conversion rate of 48.3 $\mu mol_{CO2} \cdot g_{Fe}^{-1} \cdot s^{-1}$. This outstanding performance was attributed to the strong metal-support interaction facilitated by oxygen-containing functional groups, which enhanced the dispersion of iron species and promoted the formation of more active phases.

In another study, Chen et al. [41] synthesized K-doped FeC_x catalysts through the carbothermal reduction of Fe-chitosan complexes. The appropriate Fe cation-to-chitosan ratio was a critical factor in catalyst preparation since it significantly influenced the bulk and surface carbide compositions. The proportion of the carbide phase was positively associated with the normalized yield of C_{2+}. Furthermore, the FeC_x catalyst core–shell structure was likely to enhance its durability.

Recently, limited efforts have been dedicated to synthesizing and directly applying iron carbide in CO_2 hydrogenation. Liu et al. [42] focused on preparing and utilizing Fe_5C_2 and K-modified Fe_5C_2 catalysts to investigate the relationship between the Fe phase, catalytic performance, and reaction pathways in CO_2 hydrogenation. Introducing the K promoter increased the selectivity of C_2 - C_4 olefins and C_{5+} hydrocarbons to above 38.0 C-mol% and 23.9 C-mol%, respectively, at a similar CO_2 conversion. In another study, the same research group used a combination of pure Fe_5C_2 and K-modified catalysts for the hydrogenation of CO_2. These mixture catalysts demonstrated exceptional catalytic activity, surpassing most iron-based catalysts, even without pre-reduction before the reaction. The best support for achieving high selectivity in hydrocarbons production was alkaline Al_2O_3 (a-Al_2O_3). The close interaction between Fe_5C_2 and K/a-Al_2O_3 proved crucial for the catalytic performance. Specifically, the Fe_5C_2-10 K/a-Al_2O_3 catalyst achieved a CO_2 conversion rate of 40.9 %, yielding 68.4 % of valuable hydrocarbons [43].

Inspired by the challenges mentioned earlier, in this study, the feasibility of tunning product distribution in CO_2 FTS is investigated through adjustments to the structural properties of Na-Fe_3O_4/Fe_5C_2 catalysts. The catalytic performance of Na-Fe_3O_4, Fe_5C_2, and their physical mixture is evaluated at various mass ratios, proximities, and with/without reduction treatments. Specifically, the optimal Na-Fe_3O_4 to Fe_5C_2 ratio is explored to enhance the production efficiency of C_2-C_4 olefins and C_{5+} hydrocarbons. Moreover, the impact of different spatial arrangements between active Na-Fe_3O_4 and Fe_5C_2 is analyzed. Additionally, the effects of reducing the mixed oxide/carbide on the carbon shell/layers are investigated to optimize hydrocarbon distribution. Finally, the synergistic interactions between the oxide and carbide components, which enhanced CO_2 hydrogenation performance and facilitated chain growth, have been elucidated.

2. Experimental section

2.1. Preparation of Fe_5C_2

Iron oxalate dihydrate powder was used after drying overnight at 80 °C. 1 gr of the powder was transferred into a quartz reactor with a furnace and activated to Fe_5C_2 at 350 °C under CO/He with the 10/90 mL min^{-1} flow rate for 4 h, following the method outlined by Liu et al.

[42,43].

2.2. Preparation of Fe_3O_4

A pure Fe_3O_4 catalyst was synthesized using the co-precipitation method, following the procedure described by Wen et al. [44]. Initially, $FeCl_2{\cdot}4H_2O$ and $FeCl_3{\cdot}6H_2O$ were dissolved in 0.3 mol/L HCl. Then, the ammonia water was added into the above solution dropwise while stirring until the pH of the resulting suspension reached 10. After aging at 60 °C for 60 min, the black precipitate was separated using a magnetic device and washed three times with deionized water. Finally, pure Fe_3O_4 was obtained after overnight drying at 80 °C. The 1 wt% Na-promoted Fe_3O_4 was prepared using the impregnation method. Typically, $NaNO_3$ was mixed with H_2O, and pure Fe_3O_4 was introduced into this mixture. The suspension was sonicated for 30 min and left standing for 4 h; this process was repeated thrice. The solvent evaporated, and the sample was dried overnight at 80 °C. Following this, Na-Fe_3O_4 was calcined at 350 °C for 4 h. The actual Na content of these samples was determined through EDS (Energy Dispersive Spectroscopy) analysis.

2.3. Catalyst characterizations

2.3.1. Powder X-ray diffraction (XRD)

XRD studies of all samples were performed on a Rigaku MiniFlex II instrument with a Ni-filtered CuKα source in the range of $2\theta = 10–90°$ for Na-Fe_3O_4 and Na-Fe_3O_4/Fe_5C_2 and $2\theta = 30–60°$ for Fe_5C_2. For recording the XRD patterns of the reduced sample, a PW 1830 diffractometer (Philips) using Cu Kα radiation operated in Bragg–Brentano geometry with a Ni filter at a voltage of 40 kV and a current of 30 mA was used.

2.3.2. Transmission electron microscopy (TEM)

Samples imaging was conducted with an FEI TECNAI G2 20 X-Twin high-resolution transmission electron microscope, equipped with electron diffraction, operating at an accelerating voltage of 200 kV. The surface properties, specific surface area, and pore size distributions were investigated using a Quantachrome NOVA 3000e gas sorption instrument by N_2 adsorption at liquid N_2 temperature.

2.3.3. Temperature-programmed reduction (TPR)

TPR was carried out in a BELCAT-A apparatus using an externally heated reactor (quartz tube with 9 mm outer diameter). Before the measurements, the catalyst samples were heated in He flowing at 150 °C for 60 min. Then, the sample was cooled in flowing He to 50 °C. The sample was flushed, the reactor was heated linearly at a rate of 5 °C/min from 700 °C, and the H_2 consumption was detected by a thermal conductivity detector (TCD).

2.3.4. Temperature-programmed desorption (TPD)

TPD was carried out in a BELCAT-A apparatus. Prior to the measurement, about 100 mg of the sample was pretreated in He flow at 150 °C for 60 min. After cooling to 50 °C, the sample was exposed to CO_2 and flushed in He to remove all physically adsorbed molecules. The TPD program was initiated by heating up to 700 °C with a ramp of 5 °C/min, and the CO_2 consumption was detected by TCD.

2.3.5. X-ray photoelectron spectroscopy (XPS)

The Fe-carbide samples were prepared for measurement with double-sided carbon tape on a stainless-steel sample holder. A Specs XPS instrument equipped with an XR50 dual anode X-ray source and a Phoibos 150 hemispherical analyzer was used for the measurement. The X-ray gun was operated with 150 W power (14 keV). No sample charging was observed. A survey spectrum was collected with a pass energy of 40 eV and 1 eV step size. High-resolution spectra of C, Fe, Na, and O were collected with a pass energy of 20 eV and 0.1 eV step size. Data was evaluated with CasaXPS software version 2.3.22PR1.0. All high-resolution spectra were corrected with a Shirley background. All peaks were fitted with a Gauss-Lorentzian product function, where the Lorentzian contribution is 30 %, except Fe_5C_2 peaks, which have an asymmetric peak shape.

2.3.6. Temperature-programmed hydrogenation (TPH)

For TPH analysis, the reactor outlet was connected to a mass spectrometer (UGA series). Two sets of experiments were conducted on Na-Fe_3O_4/Fe_5C_2: (1) TPH spectra were obtained after pretreatment in H_2 at 350 °C and 1 atm followed by reaction at 340 °C and 30 bar in $H_2/CO_2 = 3$ and (2) TPH spectra were collected after heating the sample in N_2 to 350 °C and 1 atm followed by reaction at 340 °C and 30 bar in $H_2/CO_2 = 3$.

In each TPH experiment, 500 mg of calcined catalyst was loaded into a stainless-steel reactor. The temperature was then increased to 350 °C at a ramp of 1 °C/min, following which a flow of pretreatment gas at 1 atm was introduced, and the reactor temperature was held at 350 °C for a specified period. Then, the temperature was reduced to 340 °C following the reaction. Following pretreatment and reaction, the catalyst was cooled in Ar to room temperature, and the gas was switched to H_2 at 1 atm while the temperature was increased to 800 °C at 5 °C/min. CH_4 was monitored using mass signals (m/z) of 15 (CH_3 fragments of CH_4) instead of 16 to avoid the interference of water vapor and CO_2 cracking.

2.3.7. In situ diffuse reflectance infrared Fourier transform spectroscopy (DRIFTS)

Infrared spectroscopy measurements were carried out with an "Agilent Cary-670" Fourier transform infrared (FTIR) spectrometer equipped with a "Harrick Praying Mantis" diffuse reflectance attachment. The sample holder had two BaF_2 windows in the infrared path. The spectrometer was purged with dry nitrogen. The spectrum of the pretreated catalyst was used as background. At room temperature, a CO_2 to H_2 mixture with a molar ratio of 1:3 was introduced into the DRIFTS cell. The tubes were externally heated to avoid condensation. The catalyst was heated linearly under the reaction feed from room temperature to 350 °C with a heating rate of 20 °C/min. All spectra were recorded in the range of 4000 to 900 cm^{-1} with a resolution of 2 cm^{-1}. Typically, 32 scans were performed. Due to the short optical path within the DRIFTS cell, the contribution of reactant gases was negligible. Only the most intense features of gas-phase products were observable.

2.3.8. Isotope exchange experiments

The catalyst (50 mg) was loaded into a fixed-bed reactor and initially reduced at 350 °C under H_2 for 2 h. Hereafter, the reactor was cooled down to 320 °C in Ar. The isotope exchange tests were performed using CO_2:H_2:Ar = 1:7:0.5 feed at 2 bar. After achieving a steady-state condition, the CO_2 was replaced by the labeled $13CO_2$ for about 30 min, which was enough for the steady-state concentration of the labeled products 13CO and $13CH_4$. The reaction products were analyzed by an online gas chromatograph as well as by an online quadrupole mass spectrometer (Universal Mass Analyzer (UGA)). The following m/z values were used for the identification of different compounds: 45 ($13CO_2$), 44 ($12CO_2$), 29 (13CO), 28(12CO), 18 (H_2O), 17 ($13CH_4$), 15 ($12CH_4$), and 40 (Ar).

2.4. Catalytic performance tests

CO_2 hydrogenation to hydrocarbons was carried out in a pressurized fixed-bed flow reactor with a 9 mm inner diameter. For non-reduced (NR) samples, the catalyst bed was initially heated in a nitrogen (N_2) atmosphere before introducing the mixture of CO_2 and H_2 ($H_2/CO_2 = 3$) at temperatures ranging from 320 to 340 °C. The reactor was pressurized to 3–5 MPa with a GHSV = 4000–5000 mL $h^{-1}g_{cat}^{-1}$. The catalytic results were collected after at least 8 h on stream. In the case of reduced samples (R), the catalysts were treated in H_2 at 350 °C for 4 h. Subsequently, the

feed gas was switched to a mixture of H_2 and CO_2 under the same reaction conditions as for NR samples. The catalysts were initially heated up under N_2.

The Na-Fe_3O_4/Fe_5C_2 catalysts were packed in two different manners: mixed-powder pellets and separate pellets. For mixed-powder pellets, the appropriate amount of Na-Fe_3O_4 and Fe_5C_2 powders was physically mixed with a mortar and pestle in different mass ratios (30/70, 50/50, and 70/30). The mixture was then pressed, crushed, and sieved to produce 20–60 mesh granules. Fe_3O_4 and Fe_5C_2 were pressed, crushed, and pelleted at 20–60 mesh for separate pellets. These pellets were subsequently mixed and loaded into the fixed-bed reactor. Unless otherwise noted, all tests in Sections 3.1, 3.2, and 3.4 were conducted using mixed-powder pellets using Na-Fe_3O_4/Fe_5C_2 70/30 wt% ratio. Unless otherwise noted, all of the Na-Fe_3O_4/Fe_5C_2 were reduced for four hours in H_2. The samples without reduction are named NR-Na-Fe_3O_4/Fe_5C_2.

The products were analyzed online using a gas chromatograph. CO, CO_2, and CH_4 were analyzed using a carbon molecular sieve column (PORAPAK) with a thermal conductivity detector (TCD). CH_4 and C_2-C_8 hydrocarbons (C_{2+}) were also analyzed using a flame ionization detector (FID) with a SUPELCO column. Chromatograms of the FID and the TCD were correlated through CH_4, and the product selectivity was obtained based on carbon balance, C-mol%. The CO_2 conversion (X_{CO2}) and product selectivity (S_i) were calculated via the following equations where n is the number of moles and c is the carbon number.

$$CO_2\ Conversion\ (X_{CO2}) = 100 \times \frac{n_{CO2,in} - n_{CO2,out}}{n_{CO2,in}} \quad (1)$$

$$Product\ selectivity\ (S_i) = 100 \times \frac{cn_i \times n_{i,out}}{\sum cn_i \times n_{i,out}} \quad (2)$$

3. Results and discussion

The N_2 adsorption/desorption isotherms of both samples displayed type IV isotherm patterns with distinct hysteresis loops, as shown in Fig. S1. The Na-Fe_3O_4 sample shows a type H1 hysteresis loop, characteristic of mesoporous materials with cylindrical pores. In contrast, Fe_5C_2 exhibits an H3-type hysteresis loop, suggesting the presence of parallel plate-shaped or wedge-shaped pores [45]. Despite the small surface area and pore volume of the Fe_5C_2 samples, indicating their non-porous nature, they still demonstrate notable catalytic activity, as discussed in the next section. This underscores that the textural properties of carbides may not be the decisive factor in the RWGS-FT reaction.

The XRD pattern of the synthesized carbide is illustrated in Fig. 1(a); peaks appeared at 2θ 39.7, 40.8, 42.9, 43.7, 44.7, 45.9, and 58.3° can be assigned to Fe_5C_2 phase, which is in accordance with the JCPDS 00-036-1248, while small peaks at 42.88 and 54.4° can be attributed to Fe_3C (JCPDS 00-035-0772) [43]. Besides, XPS spectra of synthesized carbide were collected, as presented in Fig. 1(b). The peak in the Fe 2p 3/2 and 1/2 spectra at 707.2 and 710.1 eV can be ascribed to Fe_5C_2 [42]. The Fe 2P spectra of the synthesized Fe_3O_4 are provided in Fig. S2.

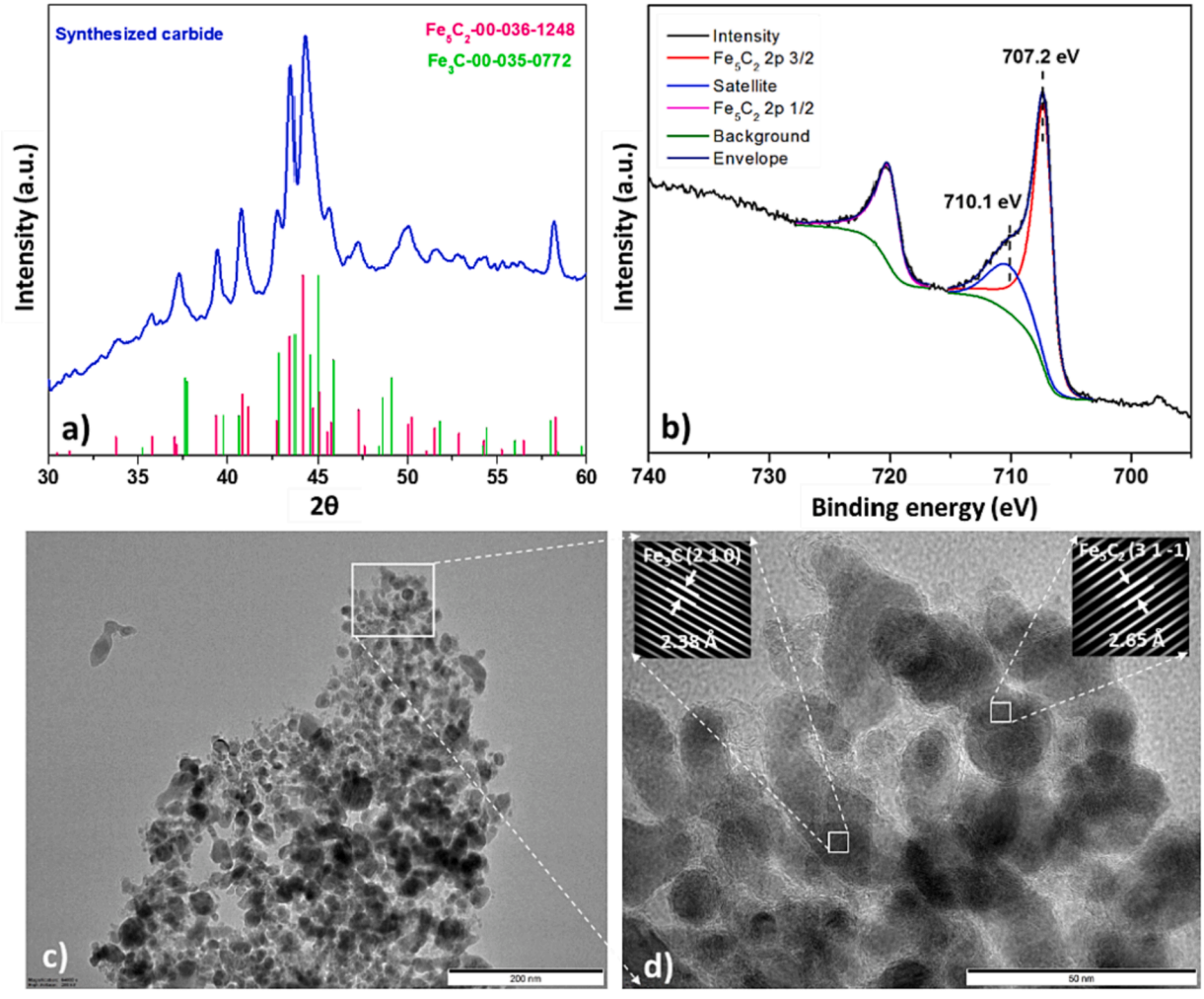

Fig. 1. a) XRD, b) XPS, and c, d) TEM images of the synthesized carbide.

The TEM images of the synthesized carbide are illustrated in Fig. 1(c) and (d) with 200 and 50 nm resolutions, respectively. The IFFT is shown in Fig. 1(d), and the fringes of Fe_5C_2 are evident in the synthesized sample.

3.1. Oxide/carbide optimized ratio

The first step to taking advantage of both Na-Fe_3O_4 and Fe_5C_2 phases is to mix them in an appropriate ratio. The ratio of oxide to carbide is an essential factor affecting the CO_2-FTS performance of Fe-based catalysts. To illustrate this point, three mixtures with different Na-Fe_3O_4/Fe_5C_2 mass ratios (30/70, 50/50, 70/30) were prepared and tested at temperatures of 320 °C and 340 °C and pressures of 30 bar and 50 bar. The results are presented in Figs. 2(a) and 2(b) in terms of C_2-C_4 and C_{5+} selectivity (including CO) versus CO_2 conversion, respectively. Each dataset was assigned a number (corresponding data are presented in Table S1); number 0 is assigned to the Na-Fe_3O_4 without mixing with carbide.

As shown in Figs. 2(a) and (b), the physical addition of Fe_5C_2 to Na-Fe_3O_4 significantly enhances CO_2 conversion (from 30 % to around 40 %). Furthermore, in both figures, the last four data points (9, 10, 11, and 12) belonging to the Na-Fe_3O_4/Fe_5C_2 ratio of 70/30 exhibit the highest yield (dashed curves in Fig. 2(a) and (b)) compared to data points with other ratios. It can also be noted that high pressure (50 bar) does not seem promising in this catalytic system, as in almost all cases, the yield didn't change considerably with increasing pressure from 30 to 50 bar (Fig. S3). It can be observed that the physical mixture of Na-Fe_3O_4 with Fe_5C_2 at a 70/30 wt ratio could improve the yield of C_2-C_4 (with an olefin/paraffin ratio of approximately 5) and C_{5+} from about 12.5 % to 17.5 % and from around 10 % to 15 %, respectively. This makes it a promising catalyst for producing light olefins, intermediates for fuel production.

The XRD patterns of Na-Fe_3O_4 and Na-Fe_3O_4/Fe_5C_2 with different ratios recorded after the reaction are presented in Fig. 2(c). The diffraction peaks at 2θ of 30, 35.33, 42.91, 56.77, and 62.25°, corresponding to the plane facets (220), (311), (200), (511), and (400), (JCPDS 01-079-0417) [46], are the characteristic peaks of Fe_3O_4 as can be observed in all the spent samples. Furthermore, the peaks corresponding to Fe_5C_2 (2θ = 40–50° (Fig. 2(d)) appeared at 2θ of 39.7, 40.8, 42.9, 43.7, 44.7, 45.9, and 58.3°, (JCPDS 00-036-1248), in the spent Na-Fe_3O_4 and Na-Fe_3O_4/Fe_5C_2 (70/30) samples. However, no peaks attributed to iron carbides can be found in the other two samples. This might be attributed to the presence of amorphous carbon shells that shielded the carbides, so they cannot be detectable by XRD, which is explained in Section 3.3. This also can be ascribed to carbide oxidation to Fe_3O_4 during the reaction. Besides, it can be observed that in the spent

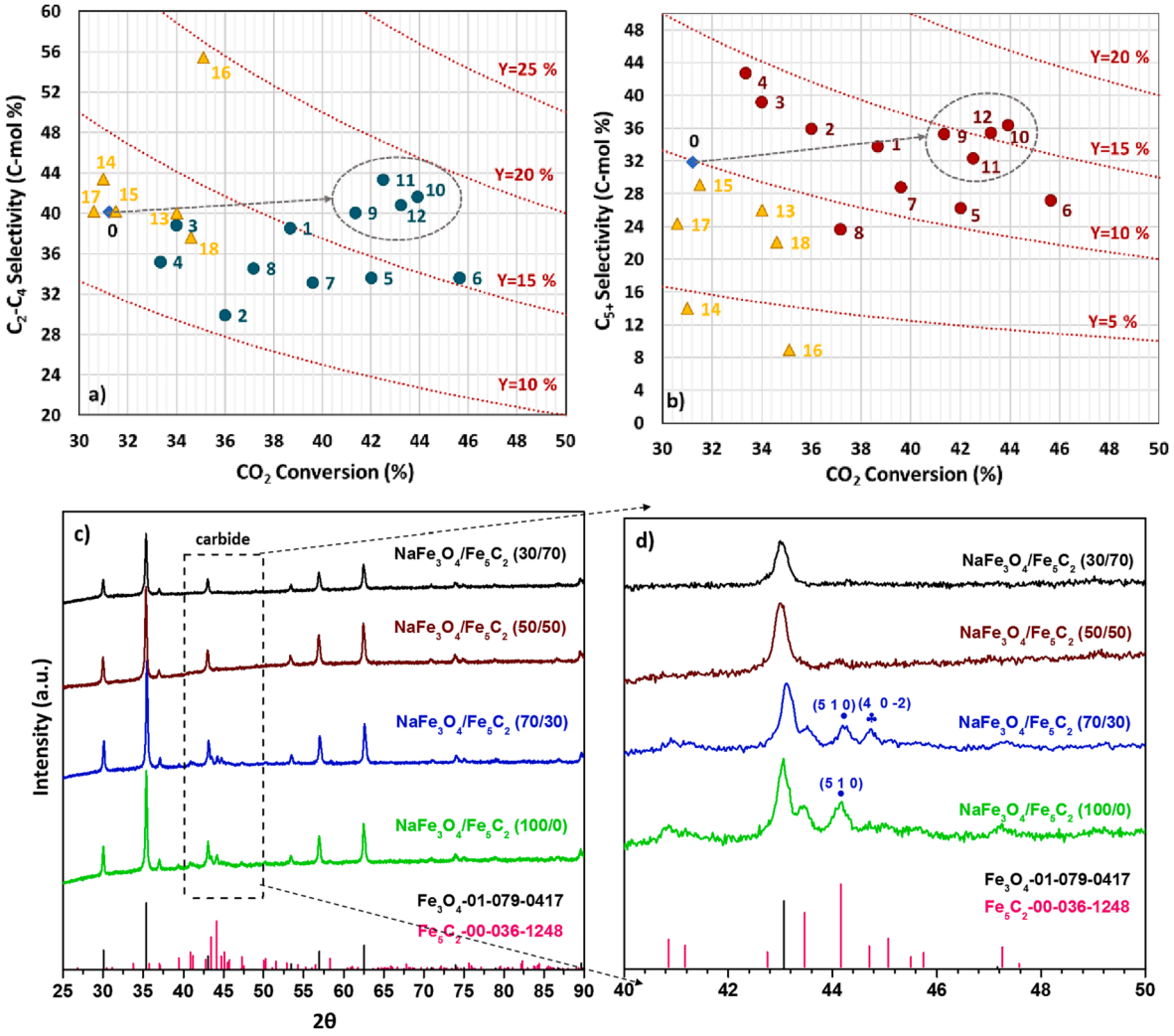

Fig. 2. Selectivity of a) C_2-C_4 and b) C_{5+} versus CO_2 conversion (Yields are shown by dashed curves. The corresponding data are presented in Table S1. The number 0 is assigned to the Na-Fe_3O_4, the numbers (1–4), (5–8) and (9–12) belong to Na-Fe_3O_4 to Fe_5C_2 with (30/70), (50/50) and (70/30) ratios, the data shown by triangles (13–18) extracted from available literature c) The XRD patterns of spent Na-Fe_3O_4/Fe_5C_2 mixed with different ratios (reaction conditions: 340 °C, 3 MPa and 4000 mL $g^{-1}h^{-1}$ GHSV, all catalysts were reduced before reaction for 4 h under H_2), d) enlarged 2θ region of the carbides.

Na-Fe_3O_4/Fe_5C_2 (70/30), the additional peak corresponds to the (4 0 −2) plane of Fe_5C_2 appeared at $2\theta = 44.71°$, while in the spent Na-Fe_3O_4 only the peak assigned to the (5 1 0) plane (at $2\theta = 44.16°$) can be detected, which is an indication of the presence of more active facets in the former catalyst.

Furthermore, it can be speculated that as the percentage of Fe_5C_2 in the mixed catalyst decreases, the intensity of peaks corresponding to Fe_3O_4 increases. This may indicate phase changes from amorphous to crystalline structures or the diffusion of more molecules into the framework of Fe_3O_4. By reducing the Na-Fe_3O_4 content in the samples (50/50 and 30/70), the presence of Na and its migration would likely decrease. Furthermore, the migration of Na^+ ions would not be facilitated due to the increased formation of amorphous carbon. This can confirm the significance of the appropriate oxide/carbide ratio in the catalyst.

To better understand the nature of active phases in the Na-Fe_3O_4/Fe_5C_2 (70/30) and Na-Fe_3O_4 samples, the XRD profiles of fresh, reduced, and spent samples are recorded and presented in Fig. 3. In the XRD pattern of Na-Fe_3O_4 (Fig. 3(a)), all the iron oxides after reduction, reduced to α-Fe, and after the reaction, the sharp peaks of Fe_3O_4 and carbides can be observed. The XRD of the Na-Fe_3O_4/Fe_5C_2 (70/30) (Fig. 3(b)) shows that the peaks corresponding to Fe_3O_4 and carbides can be observed in the fresh sample. However, in the reduced sample, the peak of metallic iron (α-Fe) appeared at $2\theta = 44.7°$, which is an indication of the reduction of a proportion of the Fe_3O_4 phase to α-Fe. Besides, the peaks of carbide and some Fe_3O_4 could still be detected in the XRD pattern of the reduced catalyst. It can be concluded that in the reduced Na-Fe_3O_4/Fe_5C_2, all of the Fe_3O_4 could not be entirely reduced to α-Fe. In the spent sample, the peaks of Fe_3O_4 and carbides are visible clearly. This shows that the metallic iron underwent carburization and was converted to carbides, while some carbides were probably oxidized, resulting in sharp peaks of Fe_3O_4. It has been shown that FeC_x could be oxidized in CO_2 hydrogenation [47]. Moreover, about 33 % Fe_3O_4 was observed in the spent sample of Fe_3O_4 promoted with 0.7 wt% Na [18].

In addition, since the peak ascribed to the plane (4 0 −2) could be detected only in the spent Na-Fe_3O_4/Fe_5C_2 (70/30), the formation of some Fe_5C_2 despite the competition between hydrogenation and carburization under a reactive environment cannot be ruled out.

Along with the ratio of Na-Fe_3O_4 to Fe_5C_2 in the initial catalyst, the integration manner of the active phases or the distance between the active sites can exert a pivotal influence on the CO_2 hydrogenation performance. To delve deeper into the performance of the mixed oxide/carbide catalyst, Na-Fe_3O_4, and Fe_5C_2 are combined using two distinct proximity modes, as elaborated in the following section.

3.2. The effect of oxide/carbide proximity

The proximity of iron carbide to the oxide phase plays a significant role in the CO_2 hydrogenation performance [2]. Pure carbide and Na-promoted Fe_3O_4 were integrated in two ways: mixed-powder pellets and separate pellet stacking, as explained in Section 2.4. In the former case, 31.7 % CH_4 was produced at a CO_2 conversion of 35.9 %, while in the latter case, the CH_4 was reduced to around 15 % at a higher CO_2 conversion. In addition, a considerable increase in C_2-C_4 olefins can be observed when the distance decreased from the separate pellet (3.5 %) to the mixed-powder pellet (38 %) mode. This underscores the importance of proximity between Na-Fe_3O_4 and Fe_5C_2 on the hydrocarbon distribution in the CO_2 hydrogenation reaction.

The increase in the amount of CH_4 and C_2-C_4 paraffins, as can be observed in Fig. 4(a), can be ascribed to the higher hydrogenation possibility when oxide and carbide are not in close contact with each other. Consequently, light olefin intermediates probably re-adsorb on the surface of the oxide, resulting in more hydrogenated products (light paraffins) when separate pellets are used in the reaction bed. Additionally, the CH_x intermediates formed over carbide could undergo hydrogenation, forming more CH_4. In contrast, the chain propagation probability is higher in the presence of mixed-powder pellets, as depicted in Fig. 4(a).

The integration manner of the two active species significantly impacts the final phases and the distribution of hydrocarbons. Fig. 4(b) demonstrates that when the oxide and carbide are closely assembled (mixed-powder pellets), XRD peaks corresponding to both Fe_3O_4 and Fe_5C_2 can be observed in the spent catalyst. However, when the distance between the two catalytically active sites is increased through separate pellet integration, the carbide peaks are no longer detectable by XRD. As explained in Section 3.1, this may be due to the oxidation of carbide to Fe_3O_4 or covering the carbide particles by an amorphous shell. This kind of carbon shell restricts the growth of catalytically active particles due to structural confinement and diffusion limitations [27]. Therefore, in separate pellets, Na^+ ions might not be able to diffuse as effectively as in the mixed-powder pellets. Furthermore, Na^+ ions can enhance the electron density and increase CO adsorption rather than H_2 adsorption, weakening the carbon–oxygen bond and improving the probability of chain propagation in the mixed-powder pellets [48]. Although both

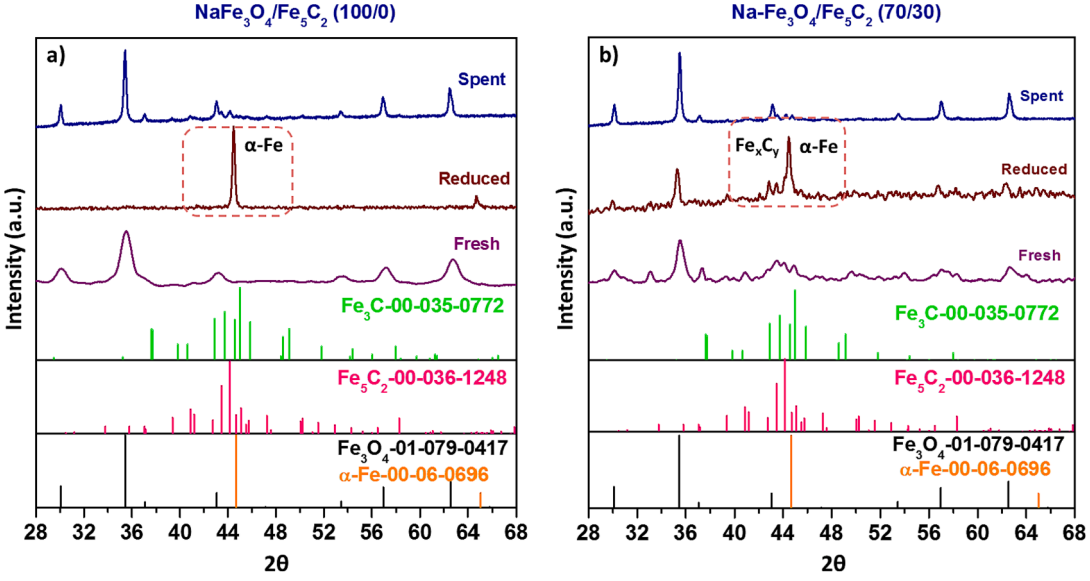

Fig. 3. XRD patterns of fresh, reduced, and spent a) Na-Fe_3O_4 and b) Na-Fe_3O_4/Fe_5C_2 (70/30).

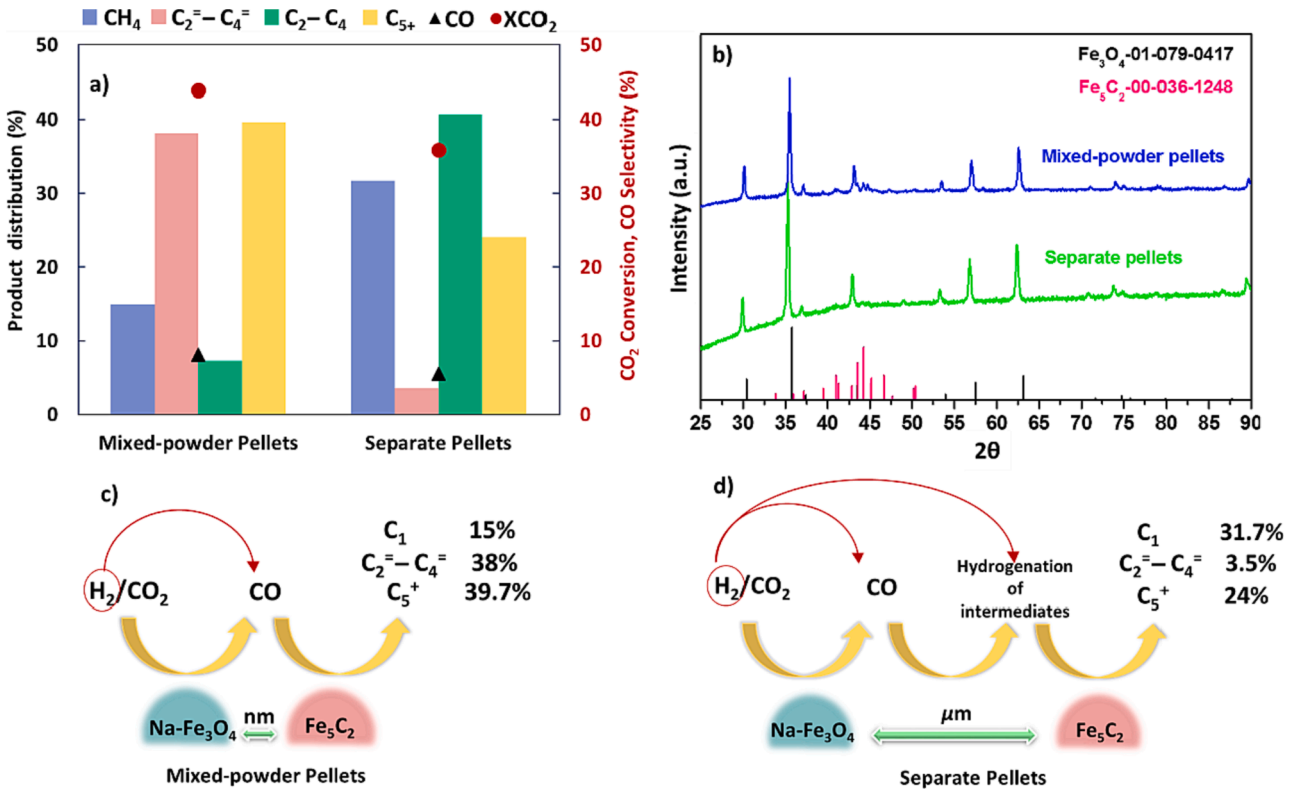

Fig. 4. a) The effect of integration manner of Na-Fe_3O_4 and Fe_5C_2 on the CO_2 hydrogenation performance at 340 °C, 3 MPa and 4000 mL $g^{-1}h^{-1}$ GHSV, b) XRD patterns of spent Na-Fe_3O_4/Fe_5C_2 (70/30 wt%) integrated in two different manners (both catalysts were reduced before reaction for 4 h under H_2), c) scheme showing the hydrocarbons distribution when the Na-Fe_3O_4 and Fe_5C_2 active sites are integrated via mixed-powder pellets, and d) separate pellets.

samples were reduced before the reaction, fewer oxygen-containing groups may be present in the separate pellets because of a higher probability of hydrogenation due to the longer distance between Na-Fe_3O_4 and Fe_5C_2.

Therefore, the boost in C_2-C_4 olefins formation in the mixed-powder pellets can be attributed to the limiting hydrogenation effects of surface carboxylate species, which allows the composite catalyst to favor C–C bonds rather than C–H at reaction temperature [49,50]. Fig. 4(c) and (d) demonstrate the scheme of the hydrocarbons distribution when the active sites are integrated with two different modes. It can be inferred that in the separate pellets, the hydrogenation of intermediates could lead to the formation of more CH_4 and saturated hydrocarbons.

After selecting the appropriate ratio and integration manner of the Na-Fe_3O_4 and Fe_5C_2, it is essential to conduct the best pretreatment to activate the catalyst and formation of the required active phases. Recent research has demonstrated that when Fe_5C_2 was included in the original catalyst, reducing the catalyst was unnecessary because the active phase was already there [42,43]. Given this issue, the following section explores the need to reduce Na-Fe_3O_4/Fe_5C_2 catalytic system before CO_2 hydrogenation reaction.

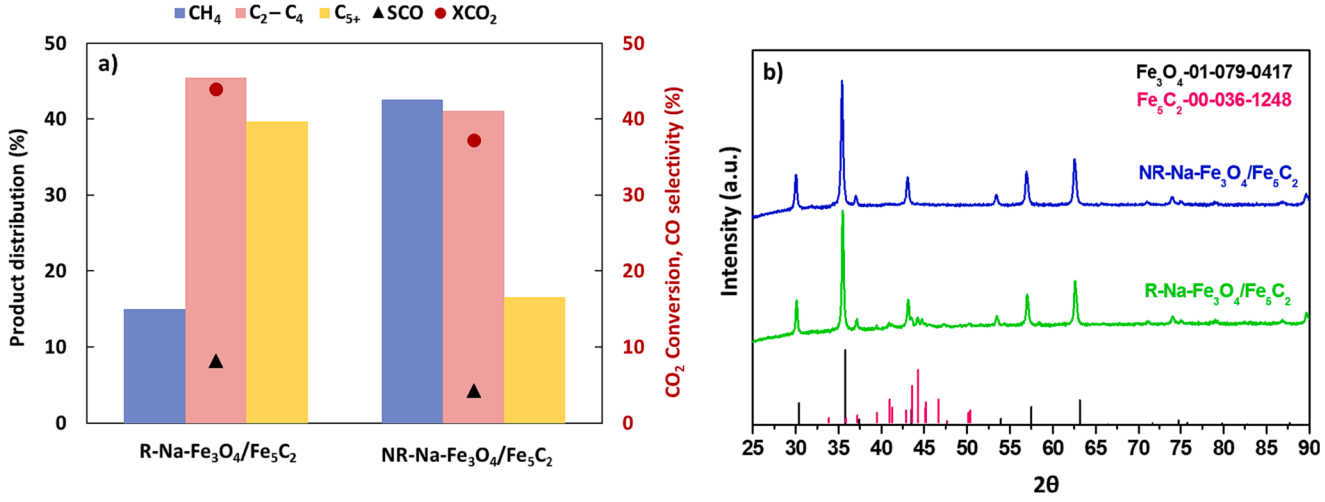

Fig. 5. a) The effect of reduction on the performance of Na-Fe_3O_4/Fe_5C_2 (70/30 wt%) at 340 °C, 3 MPa, and 4000 mL $g^{-1}h^{-1}$ GHSV and b) XRD patterns of the spent R-Na-Fe_3O_4/Fe_5C_2 and NR-Na-Fe_3O_4/Fe_5C_2.

3.3. The influence of reduction of oxide/carbide catalyst

The Na-Fe_3O_4/Fe_5C_2 samples were tested under two conditions: after reduction (R) at 350 °C and atmospheric pressure under H_2 flow and without reduction (NR) to investigate the influence of reduction on the CO_2 hydrogenation performance. When the oxide/carbide sample was not reduced (NR-Na-Fe_3O_4/Fe_5C_2), it exhibited a CO_2 conversion of about 37.2 % and a high CH_4 selectivity (approximately 43 %), as shown in Fig. 5(a). However, reduction improved the performance of both CO_2 conversion and C_{5+} selectivity (≈ 39 %), while CH_4 selectivity decreased to around 15 %. Therefore, it can be inferred that the reduction of Na-Fe_3O_4/Fe_5C_2 enhances the probability of chain propagation and reduces CH_4 formation.

The diffraction peaks of the spent samples with and without reduction are recorded and presented in Fig. 5(b). The peaks corresponding to Fe_3O_4 are observable in both samples. Furthermore, the peaks of Fe_5C_2 ($2\theta = 43–45°$) can be only detected in R-Na-Fe_3O_4/Fe_5C_2, which was reduced for 4 h before the reaction. This could be attributed to the presence of surface amorphous carbon layers concealing the carbides, thereby hindering their detection by XRD, or it could be related to the oxidation and deactivation of Fe_5C_2 during the reaction. Notably, neither increasing nor decreasing the reduction time improved the performance.

The TEM images of the R-Na-Fe_3O_4/Fe_5C_2 samples reveal that the carbide particles are encapsulated within a thick layer of graphitic carbon (Fig. 6(a–d)). However, some areas show disordered and distorted structures, along with defects in the graphitic carbon. It is plausible that, apart from reducing Fe_3O_4 to metallic Fe, some dissociated and released oxygen ions may bond with the carbon in the carbide during the reduction process. These oxygen-containing groups could increase the carbon interlayer distance, leading to the formation of graphitic layers during the reaction, as depicted in Fig. 6(b).

The migration of Na^+ can also occur during the reaction, transitioning from iron oxide to carbide. The oxygen-containing groups within the carbon interlayers might facilitate their penetration through the layers. The extensive intercalation of oxygen and Na^+ within the

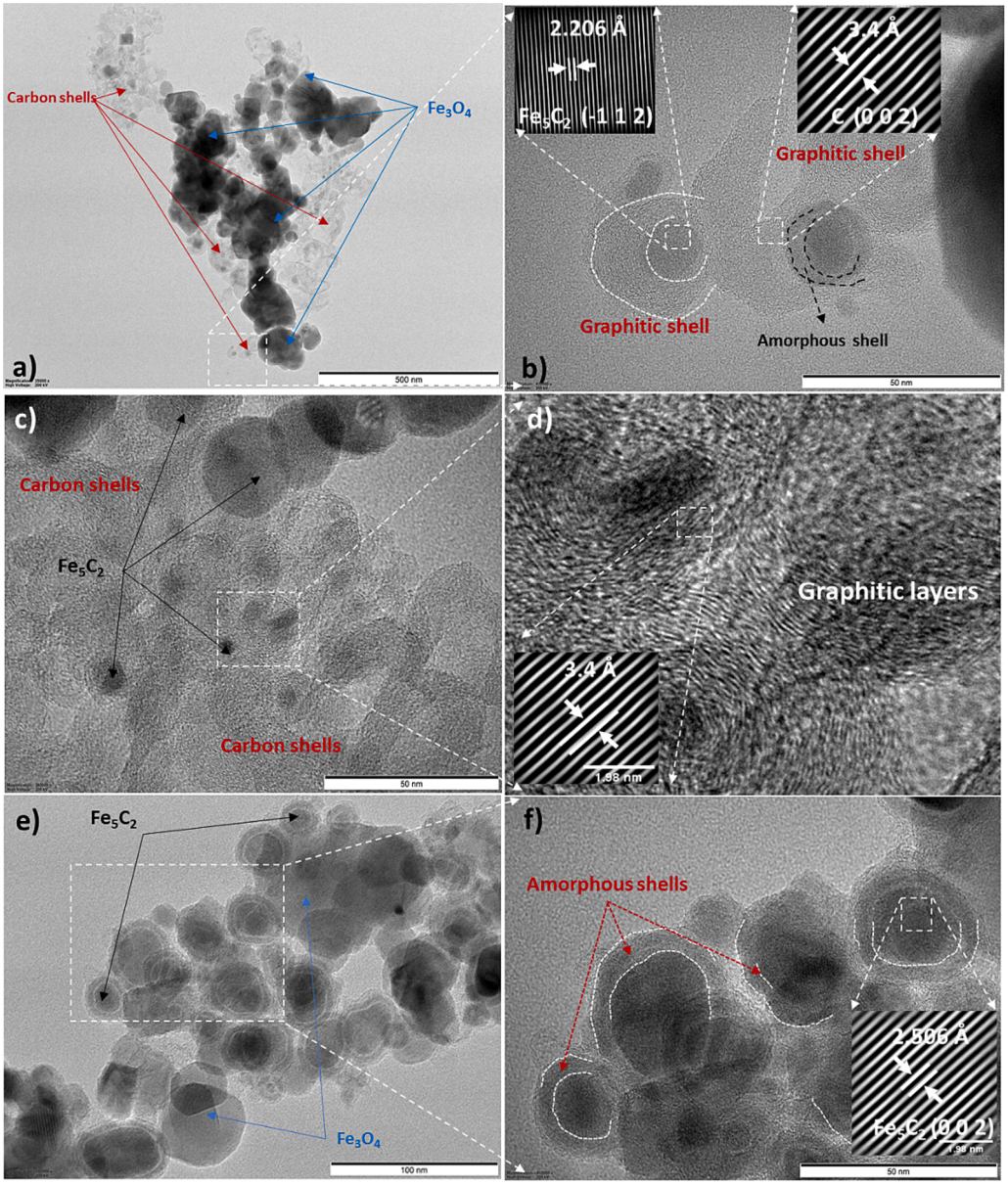

Fig. 6. a) TEM images of spent R-Na-Fe_3O_4/Fe_5C_2, b) The IFFT analysis of Fe_5C_2 and graphitic carbon along with a representation of amorphous carbon, c) Representation of distorted carbon shells, d) The IFFT analysis of graphitic carbon layers, e) TEM images of spent NR-Na-Fe_3O_4/Fe_5C_2 f) The IFFT analysis of Fe_5C_2 and representation of amorphous carbon layers.

graphite interlayers results in a more disordered pattern and defects in the graphitized shell, with only localized short-range ordering, as shown in Fig. 6(c) and (d).

In the TEM images of the spent NR-Na-Fe_3O_4/Fe_5C_2 (Fig. 6(e) and (f)), the carbides are primarily enclosed by an amorphous shell, with a small, thin graphitic carbon shell observed around them. The difference in the nature of the carbon shells in the two spent samples is likely a result of the reduction, leading to more graphitic shells around the reduced samples. This facilitated the diffusion of intermediates through the interlayer spacing of the carbon. Therefore, the TEM images of the two samples after the reaction support the hypothesis that the presence of graphitic carbon is more pronounced in the R-Na-Fe_3O_4/Fe_5C_2. At the same time, the NR-Na-Fe_3O_4/Fe_5C_2 exhibits a prevalence of amorphous carbon. He et al. [51] also showed a carbon-based confinement shell on the Fe-based nano-cube (Na-Fe@C), which led to suitable reactants/products diffusion channels on the shell. At the same time, the exposure of the active site was precisely regulated.

It can be speculated that for Na-Fe_3O_4, the carbides in the spent samples result from the carburization of metallic Fe. However, the oxides of the spent samples result from carbide oxidation. In addition, for Na-Fe_3O_4/Fe_5C_2 (Fig. 6), carbides might be those that were formed via carburization of α-Fe plus a proportion of the introduced carbide via physical mixing, which was not oxidized during the reaction according to the XRD analysis in Section 3.1.

Since XRD analysis primarily provides information about bulk phases, XPS analysis examines the surface species. The survey of the reduced and non-reduced samples is illustrated in Fig. 7(a). It can be observed that the Na/C ratio on the surface of R-Na-Fe_3O_4/Fe_5C_2 is about 1.76 %, which is approximately 1.3 times higher than that of NR-Na-Fe_3O_4/Fe_5C_2 (1.4 %). In Fig. 7(b), the divalent Fe (Fe^{2+}, Fe 2p 3/2 at 710.7 eV and Fe 2p 1/2 at 724.3 eV), and trivalent Fe (Fe^{3+}, Fe 2p 3/2 at 713.3 eV and Fe 2p 1/2 at 726.6 eV) were detected in both of the spent catalysts, indicating the presence of surface iron oxides [52] (The reference Fe 2P spectra of the synthesized Fe_3O_4 is provided in Fig. S2). A peak at approximately 707.3 and 721.7 eV can also be attributed to iron carbide species [53]. It is noticeable that the peaks corresponding to Fe^{2+} and carbide are more prominent in the R-Na-Fe_3O_4/Fe_5C_2 sample, indicating a higher concentration of surface oxide and carbide on the reduced sample after reduction. However, the surface composition of Fe^{2+}, Fe^{3+}, and Fe_5C_2 in the R-Na-Fe_3O_4/Fe_5C_2 and NR-Na-Fe_3O_4/Fe_5C_2 samples are 72.91 %, 20.64 %, 6.45 % and 73.09 %, 21.38 %, and 5.53 %, respectively. Regarding the C 1s XPS spectra (Fig. 7(c)), the primary contributions come from C–C/C–H aliphatic species, while the smaller peaks in both spectra can be assigned to C–O/C=O from adsorbed hydrocarbons [54]. The graphitic peak at 284.3 eV can be observed in the C 1s spectra [55], confirming the boost in C_2-C_4 olefins formation due to facilitated transport of the intermediates in the confined graphitic channels.

To find a deep insight into the role of reduction on the catalytic behavior of the samples, carbonaceous species of the R-Na-Fe_3O_4/Fe_5C_2 and NR-Na-Fe_3O_4/Fe_5C_2 catalysts were studied by the TPH/MS analysis. TPH spectra show a methane evolution rate due to the reaction of carbon in the spent samples with H_2, as illustrated in Fig. 8(a). According to the data in Fig. 8, it is evident that the temperature of the most intense peak increases for R-Na-Fe_3O_4/Fe_5C_2, which is an indication of strongly adsorbed carbons. However, in NR-Na-Fe_3O_4/Fe_5C_2, the main proportion of the peak appeared at temperatures lower than 700 °C, demonstrating lower graphitic layers and higher carbide content, as shown in Fig. 8(b).

The hydrogen adsorbed on NR-Na-Fe_3O_4/Fe_5C_2 is higher than that on R-Na-Fe_3O_4/Fe_5C_2 due to its sharp peak and lower peak temperature (Fig. 8(a)). It has been demonstrated that graphene-like nanosheets with a lower degree of graphitization exhibit a larger capacity for hydrogen adsorption [56]. Consequently, the higher hydrogen adsorption capacity on NR-Na-Fe_3O_4/Fe_5C_2 is attributed to its lower graphitic shell content. The substantial hydrogen adsorption on NR-Na-Fe_3O_4/Fe_5C_2 leads to an elevated H_2/CO ratio on the active sites, thereby facilitating the hydrogenation of reaction intermediates and impeding the formation of CH_x [51,57].

Shifts in peak temperature due to the pretreatment environment are also observable in the individual peak contributions of various carbon species, as illustrated in Fig. S4. The deconvoluted spectra reveal that the spectra of NR-Na-Fe_3O_4/Fe_5C_2 were best fitted by seven peaks, whereas the spectra of R-Na-Fe_3O_4/Fe_5C_2 could be well fitted by eight peaks. These peaks can be assigned to adsorbed/ atomic carbon (α), amorphous surface methylene chains or films (β), bulk iron carbide (γ), and graphitic carbon (δ). The corresponding peak temperatures and fractional peak areas are tabulated in Table S2. Notably, the peak temperatures follow a specific order, namely, in the order of decreasing reactivity with H_2 [58].

It can be observed that the low-temperature spectra of the NR-Na-Fe_3O_4/Fe_5C_2 could be deconvoluted to 4 peaks (Fig. S4(a)), while that of R-Na-Fe_3O_4/Fe_5C_2 could be separated into 3 peaks (Fig. S4(b)). The first 3 peaks in both samples can be attributed to the adsorbed atomic carbons (carbidic). However, the 4th peak in R-Na-Fe_3O_4/Fe_5C_2 and the last two (4th and 5th) peaks in NR-Na-Fe_3O_4/Fe_5C_2 can be ascribed to the amorphous carbon.

In addition, the high-temperature TPH spectra of both catalysts (Fig. S4(c), (d)) were best deconvoluted into 5 peaks, comprising 3 carbides and 2 graphitic carbons. The first two carbide peaks of R-Na-Fe_3O_4/Fe_5C_2 can be attributed to Fe_5C_2 with different morphologies, where their hydrogenation resulted in peaks around 571 and 615 °C. In

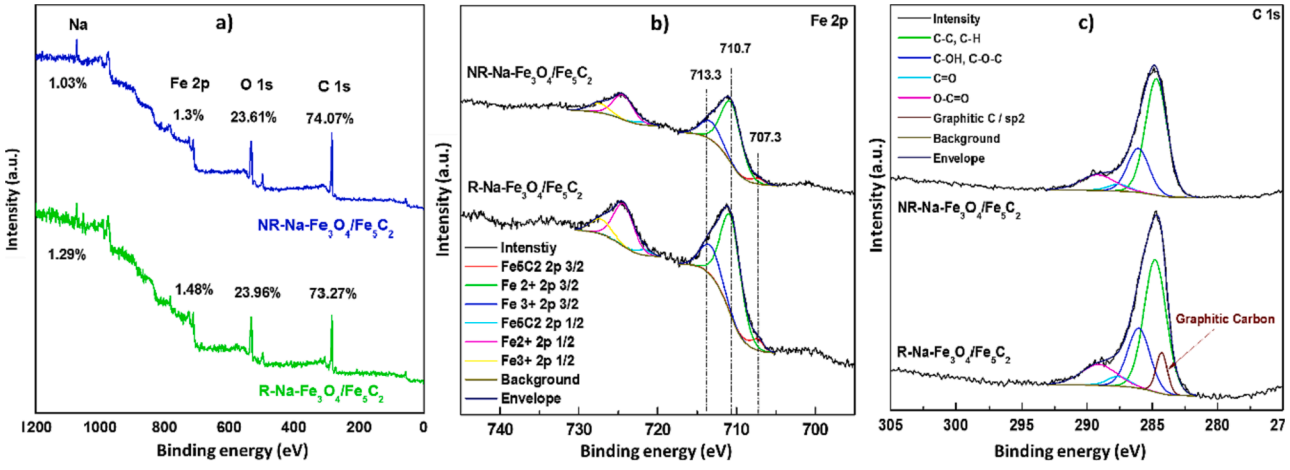

Fig. 7. XPS spectra of the spent R-Na-Fe_3O_4/Fe_5C_2 and NR-Na-Fe_3O_4/Fe_5C_2 a) Survey, b) Fe 2p, and c) C 1s.

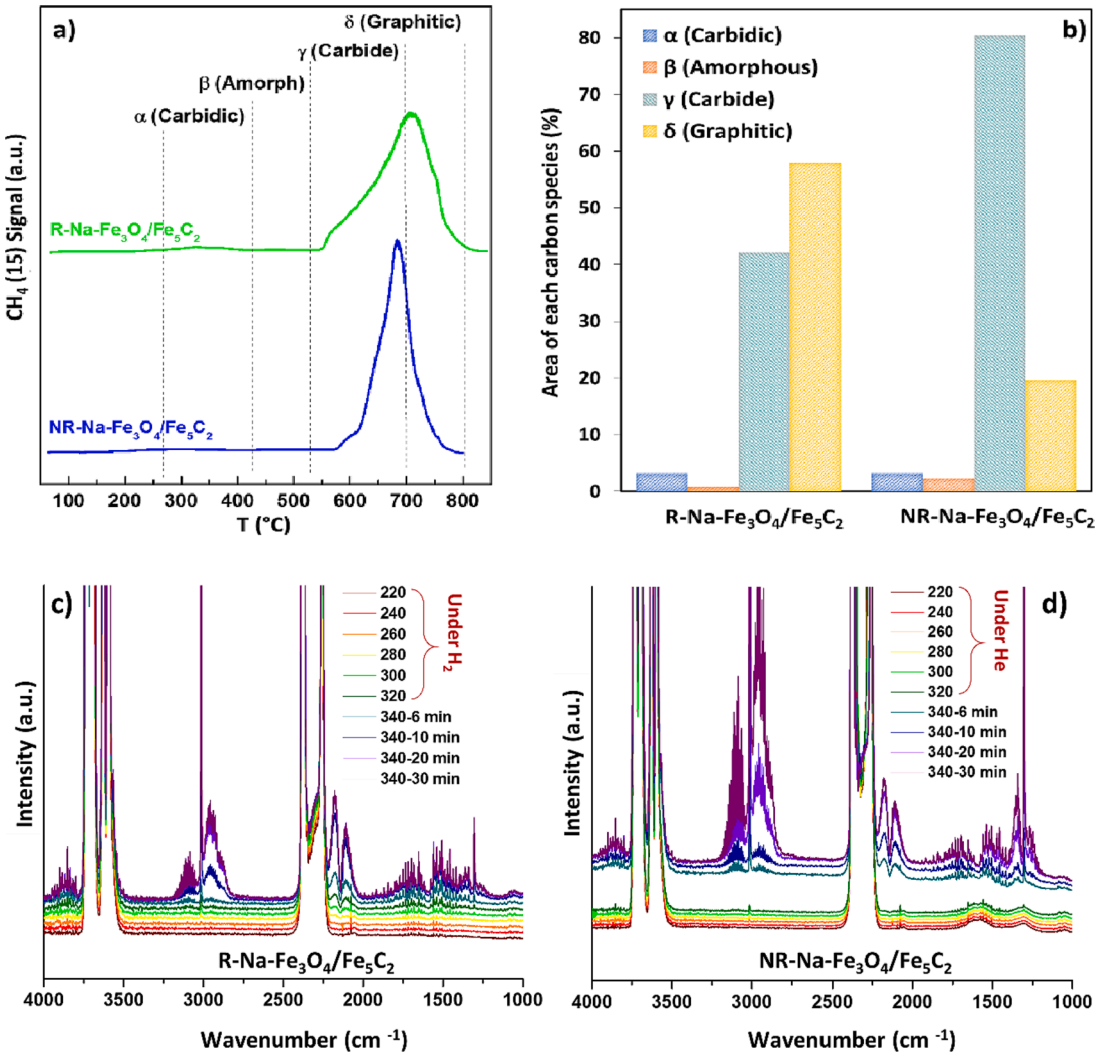

Fig. 8. a) TPH/MS spectra of spent R-Na-Fe_3O_4/Fe_5C_2 and NR-Na-Fe_3O_4/Fe_5C_2, b) The corresponding area of each carbon species in each catalyst. In-situ DRIFTS spectra obtained during CO_2 hydrogenation at 30 bar over c) R-Na-Fe_3O_4 and d) NR-Na-Fe_3O_4/Fe_5C_2.

contrast, the corresponding methane peaks of NR-Na-Fe_3O_4/Fe_5C_2 emerged at higher temperatures, approximately 599 and 655 °C.

Furthermore, the peak area of the corresponding peaks is larger in the former catalyst. In this context, it can be speculated that the lower performance of the NR-Na-Fe_3O_4/Fe_5C_2 catalyst in CO_2 hydrogenation toward C_{5+} (Fig. 5(a)) can be attributed to the weaker reactivity of Fe_5C_2 with H_2 in this catalyst. The third carbide peak is likely Fe_3C, appearing at around 670 and 687 °C in the TPH profiles of R-Na-Fe_3O_4/Fe_5C_2 and NR-Na-Fe_3O_4/Fe_5C_2, respectively. However, the contribution of Fe_3C in NR-Na-Fe_3O_4/Fe_5C_2 is significantly larger than that in R-Na-Fe_3O_4/Fe_5C_2.

The hydrogenation of graphitic carbon can lead to the formation of CH_4 at temperatures above 700 °C [59]. The corresponding peaks are larger in the R-Na-Fe_3O_4/Fe_5C_2. This observation is consistent with the presence of a graphitic peak in the C 1s XPS spectra of the R-Na-Fe_3O_4/Fe_5C_2 (Fig. 7(c)) and aligns with the TEM images of the same sample (Fig. 6(b) and (d)), revealing the increased formation of graphitic shells in the R-Na-Fe_3O_4/Fe_5C_2 after the reaction.

In this context, it can be speculated that reduction in H_2 before reaction plays a significant role in forming more graphitic shells during CO_2 hydrogenation, as observed in TEM and confirmed by XPS and TPH analysis. In addition, exposing the sample to the reactive gas (H_2/CO_2) without reduction in H_2 can result in the formation of more amorphous shells.

It is noteworthy that there is a competition between carburization and hydrogenation during FTS, which may prevent the carbonaceous species from fully covering the catalyst [59]. Moreover, the morphology of non-reduced catalyst (NR-Na-Fe_3O_4/Fe_5C_2) showed that carbonaceous species mainly appeared in the amorphous and carbide form.

Additional understanding regarding the surface species was obtained through DRIFTS experiments conducted at 30 bar, The R-Na-Fe_3O_4/Fe_5C_2 initially reduced in H_2 at 350 °C and cooled to reaction temperature, while the NR-Na-Fe_3O_4/Fe_5C_2 heated in He to the reaction temperature (340 °C), exposed to the feed gas ($H_2/CO_2 = 3$) and pressurized to 30 bar. The spectra were collected during pretreatment each 1 min, and during the reaction, four spectra (at 6, 10, 20, and 30 min) were collected in each case and illustrated in Fig. 8(c) and (d).

Consistent with steady-state catalytic results (Fig. 5(a)), NR-Na-Fe_3O_4/Fe_5C_2 exhibits more significant activity in CH_4 formation (main bands centered at 3015 and 1305 cm^{-1} [60]) compared to R-Na-Fe_3O_4/Fe_5C_2. In addition, the spectrum of both R-Na-Fe_3O_4/Fe_5C_2 and NR-Na-Fe_3O_4/Fe_5C_2 display an asymmetry in the rotational bands of CH_4 within the ν(C–H) region. This asymmetry is evident and is attributed to C–H bands from other potential products in the same area [58]. However, C–H bands are pretty weak in the FTIR spectra collected over the R-Na-Fe_3O_4/Fe_5C_2 catalyst (Fig. 8(c)). Consequently, it is evident that the type and concentration of surface CH-containing species might differ between the reduced and non-reduced catalysts. The more significant

bands at 2875–2990 cm^{-1} can be attributed to additional alkane species [60], as supported by the TPH analysis, which indicates the high hydrogen adsorption capacity of the NR-Na-Fe_3O_4/Fe_5C_2.

In summary, our findings suggest that the pretreatment environment of Na-Fe_3O_4/Fe_5C_2 catalyst influences the nature of carbonaceous species and particularly the carbon shell under CO_2-FTS conditions. The R-Na-Fe_3O_4/Fe_5C_2 exhibits a more graphitic shell, while the sample without reduction displays more amorphous carbon. The carbon shell with a higher graphitic nature exhibits a lower H_2/CO ratio around the active sites, resulting from a weaker adsorption capacity of the corresponding carbides for H_2, as shown in Fig. 8 and Fig. S4. This can reduce selectivity toward CH_4 and enhance carbon chain growth [57]. The formation of more CH_4 and hydrogenated products could also be confirmed by DRIFTS studies.

3.4. Synergistic improvement in catalytic performance of oxide/carbide

The CO_2 hydrogenation performance of pure Fe_5C_2 and Na-Fe_3O_4 is illustrated in Fig. 9(a). It can be observed that in the presence of pure carbide, CH_4 is the main product [21], constituting approximately 42 % of the total products, followed by C_2-C_4 hydrocarbons with an olefin/paraffin ratio of approximately 3 to 4. In contrast, Na-Fe_3O_4 yields more C_2-C_4 and C_{5+} hydrocarbons. However, it's worth noting that the CO_2 conversion over Fe_5C_2 (37.5 %) is higher than that of Na-Fe_3O_4 (31.2 %). Therefore, Fe_5C_2 can be considered an active phase for C=O bond activation and CH_x hydrogenation. It has been revealed that the structure of Fe_5C_2 is critical for its interaction with CO_2, H_2, and CO. Defective Fe_5C_2 favors efficient CO_2 and CO adsorption [61].

Comparing the performance of these two catalysts with their physical mixture, it can be speculated that the mixed catalyst outperforms the individual components in terms of selectivity toward C_{5+} hydrocarbons (about 39 % excluding CO) while producing lower amounts of CO compared to that of Na-Fe_3O_4. Increased CO_2 conversion and decreased CO selectivity resulted in a higher C_{5+} yield, approximately 16 %, over the Na-Fe_3O_4/Fe_5C_2 mixture (Fig. 9(a) green columns). This might be due to the transformation of more CO toward light olefins and C_{5+} hydrocarbons due to the presence of Fe_5C_2 in the initial catalyst. Interestingly, it can be observed that using pure Fe_5C_2 inhibits the conversion of C_2-C_4 olefins into C_{5+} hydrocarbons, while the Na-Fe_3O_4/Fe_5C_2 mixture can significantly enhance chain propagation. Therefore, while Fe_5C_2 can efficiently produce valuable C_2-C_4 olefins as intermediates for C_{5+} formation, an optimal ratio and distance between oxide and carbide is necessary to inhibit further hydrogenation of intermediates and, therefore, the formation of C_{5+} hydrocarbons. The GC–MS spectra of the liquid products (Fig. S5) confirm the formation of heavier unsaturated hydrocarbons in the presence of physically mixed Na-Fe_3O_4 with Fe_5C_2. It should be mentioned that no liquid products were produced using Fe_5C_2 alone.

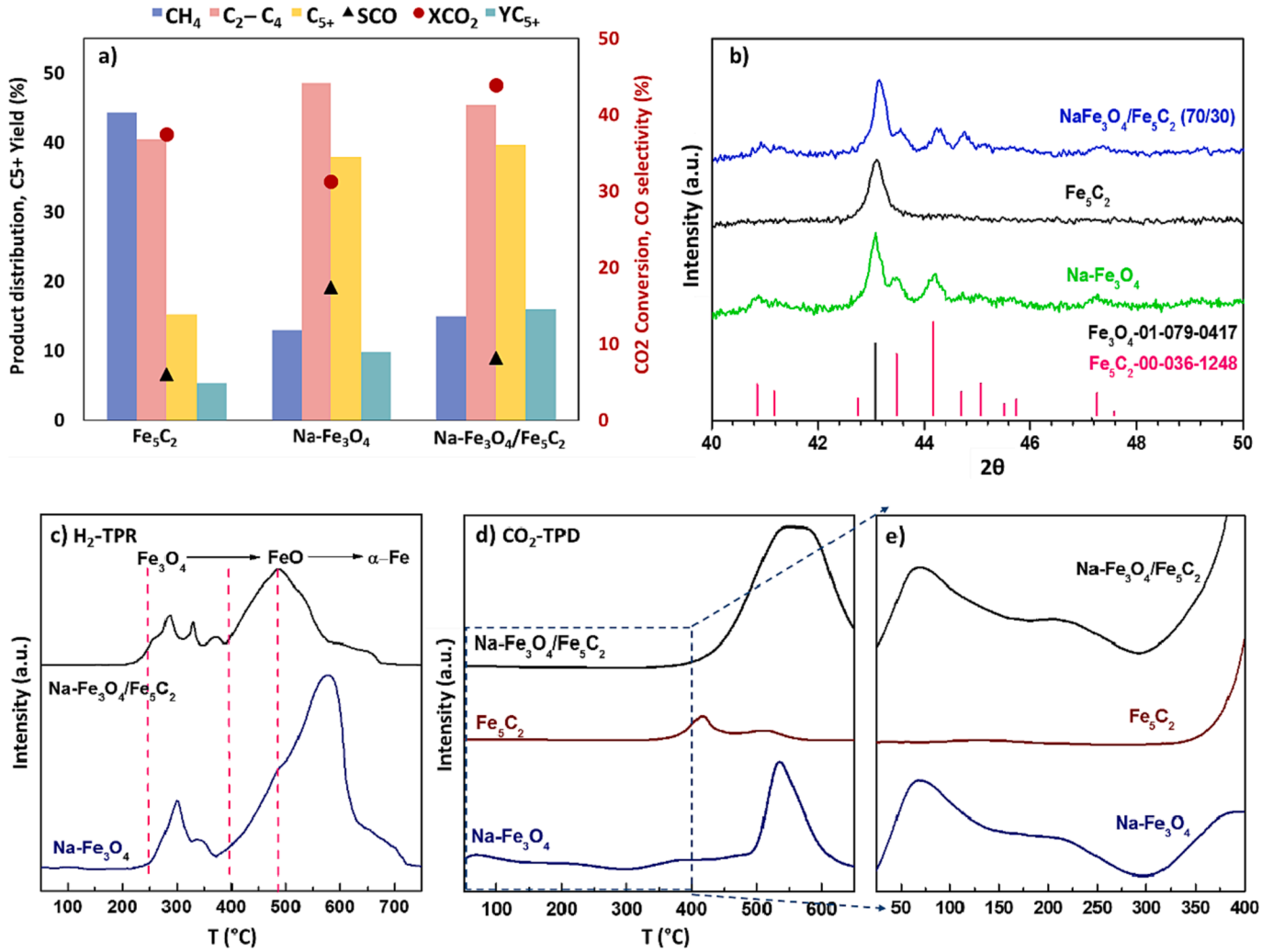

Fig. 9. a) The effect of physical mixing of Fe_5C_2 with Na-Fe_3O_4 on CO_2 hydrogenation performance and b) XRD patterns of the spent samples (reaction conditions: 340 °C, 3 MPa, and 4000 mL $g^{-1}h^{-1}$ GHSV, both catalysts were reduced before reaction for 4 hours under H_2, the catalyst used was Na-Fe_3O_4/Fe_5C_2 (70/30 wt%)). c) H_2-TPR profiles of Na-Fe_3O_4 and Na-Fe_3O_4/Fe_5C_2 (70/30), d) CO_2-TPD profiles of Na-Fe_3O_4, Fe_5C_2 and Na-Fe_3O_4/Fe_5C_2 (70/30), and e) Enlarged CO_2-TPD profile.

In order to compare the active phases in each sample, the XRD patterns of Na-Fe_3O_4, Fe_5C_2, and their mixture after reaction in the range of carbides (2θ = 40–50°) are illustrated in Fig. 9(b). The diffraction peaks of Fe_3O_4 are observed in all samples; however, no peaks corresponding to the carbide could be detected in the spent Fe_5C_2. This might be due to the oxidation of Fe_5C_2 during the CO_2 hydrogenation reaction. However, according to the XRD spectra presented in Fig. 3, the spent Na-Fe_3O_4 and Na-Fe_3O_4/Fe_5C_2 (70/30) contain Fe_5C_2. This confirms that the presence of both Na-Fe_3O_4 and Fe_5C_2 in an appropriate ratio and proximity is required to form the active phase for CO_2 hydrogenation to C_{5+} hydrocarbons.

To assess the hydrogen reduction and CO_2 adsorption capacity of the catalysts, H_2-TPR and CO_2-TPD analysis were conducted, while TGA was used to measure their thermal stability. The H_2-TPR profiles of Na-Fe_3O_4 and Na-Fe_3O_4/Fe_5C_2 samples are presented in Fig. 9(c). The Na-Fe_3O_4 profile (blue line) shows two main H_2 consumption regions, with peaks centered at 300 °C and 575 °C. Typically, the first H_2 consumption region from 250 to around 400 °C can be attributed to the reduction process of Fe_3O_4 → FeO, while the second, broader region from 400 to 750 °C may reflect the reduction of FeO → α-Fe [62]. The shoulder peak observed in Na-Fe_3O_4 at 480 °C could be attributed to the reduction of bulk Fe_3O_4 species to FeO. In contrast to Na-Fe_3O_4, the Na-Fe_3O_4/Fe_5C_2 catalyst exhibits multiple reduction peaks for the transition from Fe_3O_4 to FeO, suggesting a more distinct reduction stage in the reduction of surface Fe_3O_4 to FeO. In addition, it can be observed that the Fe_3O_4 reduction to FeO could be facilitated in Na-Fe_3O_4/Fe_5C_2, as this peak appeared at lower temperatures (around 515 °C). However, the complete reduction of Fe_3O_4 to α-Fe was hindered, as explained in section 3.1 (XRD of the reduced Na-Fe_3O_4/Fe_5C_2 catalyst (Fig. 3(b)). The decrease in peak intensity of the Na-Fe_3O_4/Fe_5C_2, notably the transition from FeO → α-Fe, could be due to the lower oxide content in the physically mixed sample (70 %) compared to Na-Fe_3O_4.

To analyze the CO_2 adsorption capability of the samples, CO_2-TPD of the fresh samples was performed as depicted in Fig. 9(d). The location of the CO_2 desorption peak and its area indicate the interaction of different Fe-oxide phases with CO_2 and the corresponding amount of these Fe-oxide phases in the sample. This provides an indication of the sample's basicity. In the Na-Fe_3O_4 profiles, a broad peak below 100 °C can be attributed to weakly adsorbed CO_2 on the catalyst surface with basic sites [63]. In comparison, a distinct peak representing strong CO_2 adsorption appears at approximately 550 °C, with no significant signs of decomposition according to the TGA (Fig. S6(a)). It can be observed that the Fe_5C_2 exhibited a small low-intensity peak at about 400 °C, which represents its lower basicity compared to that of Na-Fe_3O_4. Therefore, the Na-Fe_3O_4/Fe_5C_2 basicity arises mainly from the Na-Fe_3O_4, as observed in the corresponding CO_2-TPD spectra in Fig. 9(b). However, the sharp peak of the Na-Fe_3O_4/Fe_5C_2 mixture between 450 and 550 °C can also be due to the sample decomposition at high temperatures according to the TGA curve (Fig. S6(b)), appearing at almost the same temperatures. Therefore, this sharp peak is likely associated with sample decomposition rather than the strong adsorption of CO_2. Hence, we focused on the low-temperature range before 450 °C (Fig. 9(e)) to avoid misinterpretation. It can be inferred that the mixing of Na-Fe_3O_4 with Fe_5C_2 led to a gradual shift of these low-temperature peaks to higher temperatures. This shift suggests that CO_2 adsorbed strongly to the active sites on the Fe-based catalyst surfaces in the physical mixture of the two components (Na-Fe_3O_4 with Fe_5C_2) compared to Na-Fe_3O_4. This difference could contribute to the higher CO_2 conversion and C_{5+} yield observed.

To obtain a clear insight into the mechanism of CO_2 hydrogenation in the presence of both catalysts, operando DRIFTS was performed. To this end, after the reduction in H_2 at 350 °C, it was cooled down to room temperature. The DRIFTS cell was then pressurized with the reaction gas mixture (H_2/CO_2 = 3) to 30 bar and heated up to 340 °C with a ramp of 20 °C/min. When the temperature reached 220 °C, the DRIFTS spectra were collected each 1 min until the temperature reached 340 °C, and then, four spectra were collected at this temperature after 6, 10, 20, and 30 min of reaction time. The DRIFTS spectra of Na-Fe_3O_4 and Na-Fe_3O_4/Fe_5C_2 under CO_2 hydrogenation are illustrated in Fig. S7. To provide a better comparison, the last spectra of both samples after 30 min of reaction are illustrated in Fig. 10(a-c).

A strong band at 2400–2200 cm^{-1} is attributed to gas-phase CO_2, and two strong twin-bands observed in the range of 3750–3550 cm^{-1} correspond to the combined tones of gas and adsorbed CO_2 molecules. It can be observed that the reaction starts at almost 320 °C as the peaks of CO and CH_4 appear. The gas phase spectrum of CO has its characteristic bands between 2110 and 2177 cm^{-1}. The RWGS reaction took place on both catalysts to different extents, leading to the formation of more CO on the Na-Fe_3O_4, as can be observed in Figs. S7(b) and (e). The formation of CH_4 is clearly observable in all spectra indicated by its typical gas phase spectrum with main bands centered at 3015 and 1305 cm^{-1}.

After reaching reaction temperature (340 °C), bands assigned to carbonate species ($CO_3^{\bullet-}$, ca. 1712, 1555 and 1453 cm^{-1}), bicarbonate species ($HCO_3^{\bullet-}$, ca.1630 and 1419 and 1224 cm^{-1}) and formate species ($HCOO^{\bullet-}$, ca. 2854, 1560 and 1360 cm^{-1}) appeared in both catalysts. In addition, the C-H stretching of alkanes (2875–2990 cm^{-1}) and alkenes (3030–3180 cm^{-1}) gradually strengthened with the reaction proceeding in both samples (Fig. 10(a)). It is noteworthy that, in Na-Fe_3O_4, the bands corresponding to C-H stretching of alkanes are considerably larger than those of Na-Fe_3O_4/Fe_5C_2, which can confirm the robust hydrogenation and, therefore, the formation of more saturated compounds on Na-Fe_3O_4.

Therefore, the time profile of the reaction indicates that the mechanism for the formation of hydrocarbons is as follows: CO_2 is adsorbed onto the catalyst surface as carbonate species, and hydrogenation of this carbonate species proceeds to form bicarbonates and subsequently formate species. Then, hydrogenation of the formate produces CO by the RWGS reaction, which proceeds more on Na-Fe_3O_4, probably due to 100 % Fe_3O_4 content, while in Na-Fe_3O_4/Fe_5C_2 70 wt% of the catalyst is Fe_3O_4. Besides, the adsorbed CO is hydrogenated to form adsorbed CH_x species, ultimately yielding paraffins (to a greater extent on Na-Fe_3O_4) and olefins via the FT reaction. Since Fe_5C_2 is the active phase of FTS, it can be speculated that the presence of this phase in the Na-Fe_3O_4/Fe_5C_2 hindered extra hydrogenation of intermediates to saturated hydrocarbons, thus increasing the olefins as shown in GC–MS peaks in Fig. S5.

Considering these findings and the performance evaluations represented in Fig. 4 and Fig. 9, the following scheme can be proposed for the hydrocarbon formation in the presence of Na-Fe_3O_4/Fe_5C_2 catalyst. First, the CO_2 activation and dissociation to CO occurs on Fe_3O_4. It has been reported that the formed CO is transformed to the Fe_5C_2 surface via spillover from the oxide surface [64]. Subsequently, the adsorbed CO and H* on the carbide surface can react to produce intermediates, and chain initiation begins over Fe_5C_2. Finally, if the active sites are spatially appropriately stacked, the intermediates can induce chain propagation reactions at the interface (Fig. 10(d)), resulting in heavier unsaturated hydrocarbons. This is in agreement with the DFT calculations of Zhao et al. [65] that showed C–C coupling was easier than CH_4 formation on the Fe_5C_2 surface, which makes it highly active for FTS with high olefin selectivity.

The isotope exchange experiment was conducted to check if the carbon source in the produced hydrocarbons originated from CO_2 and not from the decomposition of the introduced Fe_5C_2 in the initial catalyst. The normalized responses are illustrated in Fig. 10(e). By switching from CO_2 to $13CO_2$, the concentration of CO_2 and CO decreased, showing that these gases were being replaced by $13CO_2$ and 13CO. In addition, the CH_4 (m/z = 15) decreased, while the $13CH_4$ started increasing due to the formation of labeled methane (m/z = 17). It should be noted that since the formation of CH_4 under low pressure was not favored, the concentration of methane was not high, which resulted in the noisy data points for methane spectra. Notably, by switching to the $13CO_2$, no more CH_4 at m/z 15 could be detected. This indicates that the $13CO_2$ only resulted in the formation of $13CH_4$ (m/z 17), and no sign of

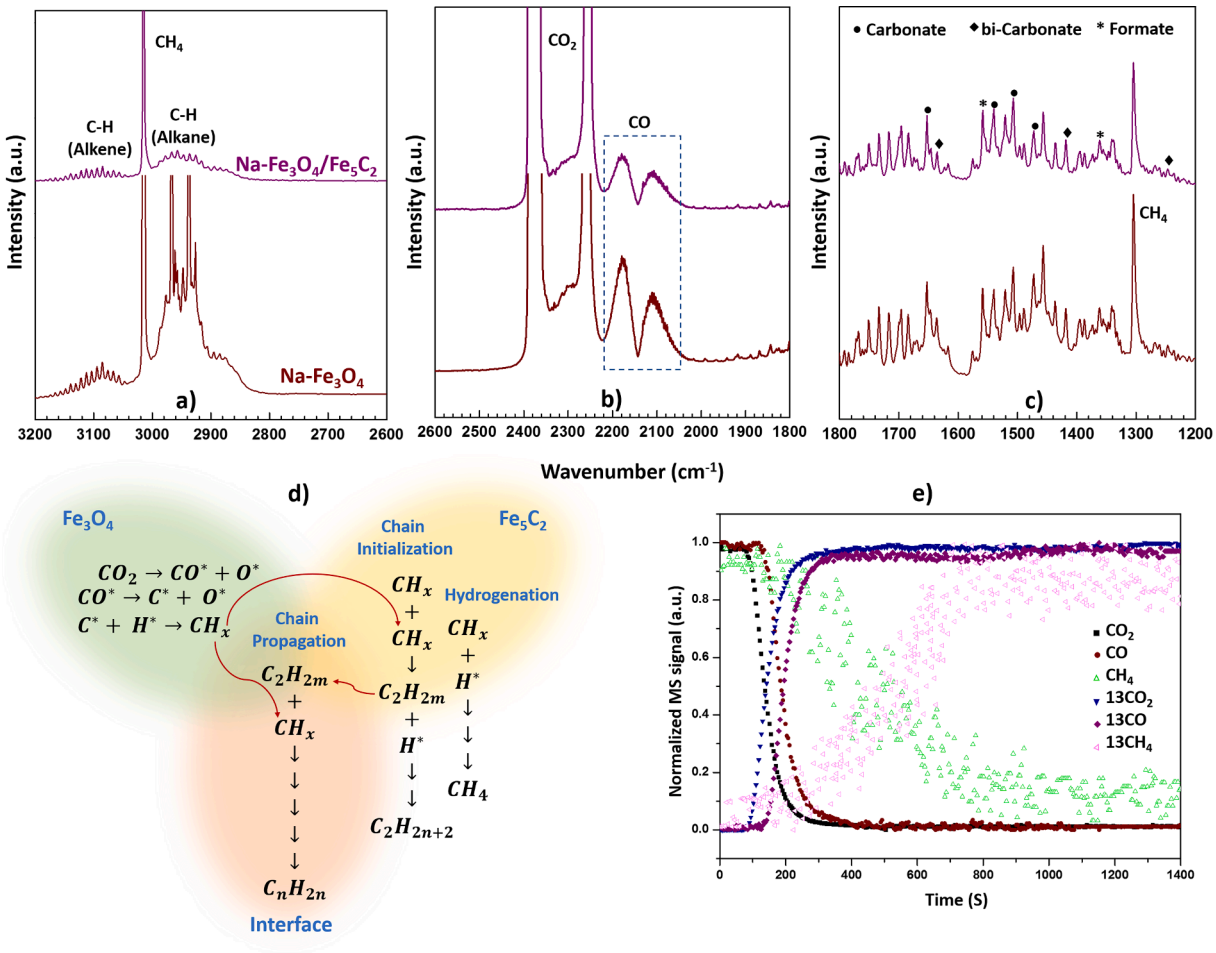

Fig. 10. a), b), and c) Comparison of DRIFTS spectra of Na-Fe_3O_4 and Na-Fe_3O_4/Fe_5C_2 (70/30) after 30 min of CO_2 hydrogenation at 340 °C and 30 bar, d) Schematic representation of the mechanism over Na-Fe_3O_4/Fe_5C_2, e) Normalized MS spectra collected during the switch from CO_2 to $13CO_2$.

CH_4 (m/z 15) could be found. These findings show that the carbon in the products originates from the $13CO_2$ dissociation and not the carbide decomposition in the initial catalyst. In one study, Ordomsky et al. [66] carburized the Fe-oxide in the 13CO environment to form the labeled carbide and analyzed the source of carbon in the products by MS. It was found that labeled carbon of carbide did not form hydrocarbons but could participate in the chain growth. Afterward, the active site might be regenerated by CO with the formation of carbide and continuation of the growing chain. The contribution of labeled carbon decreased from ethylene to butylene, which is consistent with the assumption about the participation of labeled carbon only in chain initiation.

Moreover, the long-term stability of the Na-Fe_3O_4/Fe_5C_2 catalyst was evaluated, and the results are presented in Fig. S8. It demonstrates good stability over 40 hours on stream. The products selectivity were stable, and the CO_2 conversion was marginally changed (within 2 %) during this period.

3.5. Structure-performance relationship

Iron carbides are often reported to be the primary active phase responsible for chain growth in FTS [67]. However, the results demonstrated that the pure carbide, inappropriate oxide/carbide ratio and proximity, and non-proper reduction cannot enhance the formation of long-chain hydrocarbons. Furthermore, it can be concluded that the nature of active phases and the morphology of carbon shells of carbides can be affected by the reduction treatment.

In the case of Na-Fe_3O_4 at the beginning of the reduction in H_2, the surface O atoms of Fe_3O_4 are gradually removed to form metallic iron sites (α-Fe) as supported by XRD of the reduced catalyst (Fig. 3(a) reduced). By introducing the feed gas, iron carbide forms through carbon permeation to the α-Fe sites. However, in the spent sample, the appearance of Fe_3O_4 peaks confirms the oxidation of Fe_5C_2 during the reaction (Fig. 3(a) spent).

In the presence of Na-Fe_3O_4/Fe_5C_2, at the beginning of the reduction in H_2, the same phenomenon happens, and surface O atoms of Fe_3O_4 are gradually removed to form metallic iron sites. However, the presence of 30 wt% carbide in the catalyst hindered the complete reduction of Fe_3O_4, resulting in the presence of both α-Fe and Fe_3O_4 (non-reduced) phases after reduction based on the XRD of the reduced samples (Fig. 3 (b) reduced). It has been shown that the carburization rates were controlled by the oxygen-depletion rate, and the dense iron carbide layer on the Fe_3O_4 surface provided an effective barrier to the removal of oxygen [68]. These results show that iron carbide formed a layer on some parts of Fe_3O_4 surface, impeding oxygen diffusion [33]. This is in accordance with the H_2-TPR profiles (Fig. 9(c)), which show a small peak area in the region of α-Fe formation for Na-Fe_3O_4/Fe_5C_2 compared to the sharp peak of Na-Fe_3O_4, confirming the hindrance in further reduction to α-Fe. By introducing the reaction gas (H_2/CO_2), the C atoms react with the α-Fe to form carbide. Therefore, at the onset of reaction, both Fe_5C_2 (from α-Fe carburization plus the initial carbide in the catalyst) and Fe_3O_4 (the un-reduced proportion of the initial Fe_3O_4) are present. In addition, it can be observed that some peaks of Fe_5C_2 (at $2\theta = 37.05$ and $40.86°$) disappeared after reduction, while the intensity of another peak at $2\theta = 42.75°$ increased in the spent sample (Fig. 3(b) spent).

In the non-reduced catalyst (NR-Na-Fe_3O_4/Fe_5C_2), also both Fe_3O_4

and Fe_5C_2 are present at the onset of the reaction. However, this catalyst showed poor CO_2 hydrogenation performance for producing C_2-C_4 olefins and C_{5+} hydrocarbons, as shown in Fig. 5(a). Furthermore, TEM images (Fig. 6(e) and (f)) show more amorphous carbon shells/layers in the spent samples, which is confirmed by TPH analysis (Fig. 8 and (S4)).

It was revealed that by using the Na-Fe_3O_4/Fe_5C_2 catalyst without reduction, the oxide/carbide ratio at the onset of the reaction remained intact (the same as an initial catalyst), which altered the morphology of carbon shells to more amorphous after the reaction. In addition, amorphous carbon content in the spent NR-Na-Fe_3O_4/Fe_5C_2 observed in TPH analysis (Fig. S4(d)) can confirm the shielding of the carbides surface. Besides, the higher hydrogen adsorption in the presence of amorphous shells, as shown by TPH/MS, confirms a higher H_2/CO ratio on the active sites of the non-reduced catalysts. Moreover, the thick carbon layer and carbide content can cover Fe_3O_4 and hinder oxygen depletion. Low oxygen removal ability has been shown to favor the formation of carbon-deficient Fe_3C rather than carbon-rich Fe_5C_2 [58]. Therefore, it can be concluded that some of the Fe_5C_2 transformed to carbon-deficient Fe_3C during hydrogenation.

These physicochemical properties also correlate well with the CO_2 hydrogenation performance of the catalyst, as depicted in Fig. 11(a-d). Accordingly, More C_{5+} can be achieved in the reduced catalysts (case II in Fig. 11(d)) as a result of regulated active phase ratios, while more CH_4 is obtained on non-reduced samples (case III in Fig. 11(d)) due to higher hydrogenation ability of the amorphous shells.

Therefore, reduction treatment and, in turn, morphology of the carbon shells can significantly affect the CO_2 hydrogenation performance. In this context, more graphitic carbon layers are found to be responsible for the superior performance of the R-Na-Fe_3O_4/Fe_5C_2, while the amorphous shells in the NR-Na-Fe_3O_4/Fe_5C_2 resulted in the formation of more CH_4 and saturated hydrocarbons.

4. Conclusions

Na-Fe_3O_4 and Fe_5C_2 were synthesized and physically mixed in various ratios for the CO_2 hydrogenation to C_{5+} hydrocarbons. The results showed a significant increase in CO_2 conversion, while CO selectivity decreased when carbide was physically mixed with oxide. This enhancement was attributed to the regulated reduction of the oxide phase in the Na-Fe_3O_4/Fe_5C_2 mixture and improved CO_2 adsorption.

In addition, it was revealed that the Na-Fe_3O_4/Fe_5C_2 ratio in the initial mixture significantly changed the carbide content at the onset of the reaction and, in turn, the CO_2 hydrogenation performance. Moreover, the proximity between Na-Fe_3O_4 and Fe_5C_2 played a significant role in product distribution; a closer distance resulted in higher C_2-C_4 olefins and C_{5+} selectivity, while more hydrogenated products formed when Na-Fe_3O_4 and Fe_5C_2 were stacked in separate pellets. Furthermore, the reduction of the mixed oxide/carbide improved catalytic performance, likely due to the presence of graphitic carbons with extended and distorted layers and defects. However, amorphous carbon formed in the NR-Na-Fe_3O_4/Fe_5C_2 facilitated the production of light paraffins and CH_4.

It can be deduced that the ratio of Fe_5C_2 to Fe_3O_4 at the onset of the reaction and the nature of carbon shell/layers can be tuned by the reduction treatment and adjusting the appropriate ratio of Na-Fe_3O_4 to Fe_5C_2 in the initial catalyst, as supported by the characterization of the reduced and spent samples. To sum up, the interaction of the essential variables, such as oxide/carbide ratio, proximity, and reduction treatment, may enable the development of a CO_2 hydrogenation catalyst that effectively promotes the production of valuable hydrocarbons.

CRediT authorship contribution statement

Sara Najari: Writing – original draft, Visualization, Software, Methodology, Investigation, Data curation, Conceptualization. **Samrand Saeidi:** Writing – review & editing, Visualization, Validation, Resources, Methodology, Investigation, Data curation, Conceptualization. **András Sápi:** Writing – review & editing, Supervision, Investigation, Funding acquisition. **Ákos Szamosvölgyi:** Visualization, Software, Investigation, Data curation. **Ádám Papp:** Software, Resources, Formal analysis, Data curation. **Anastasiia Efremova:** Visualization, Resources, Formal analysis, Data curation. **Henrik Bali:** Visualization, Resources, Data curation. **Zoltán Kónya:** Writing – review & editing, Supervision, Funding acquisition.

Declaration of competing interest

The authors declare that they have no known competing financial

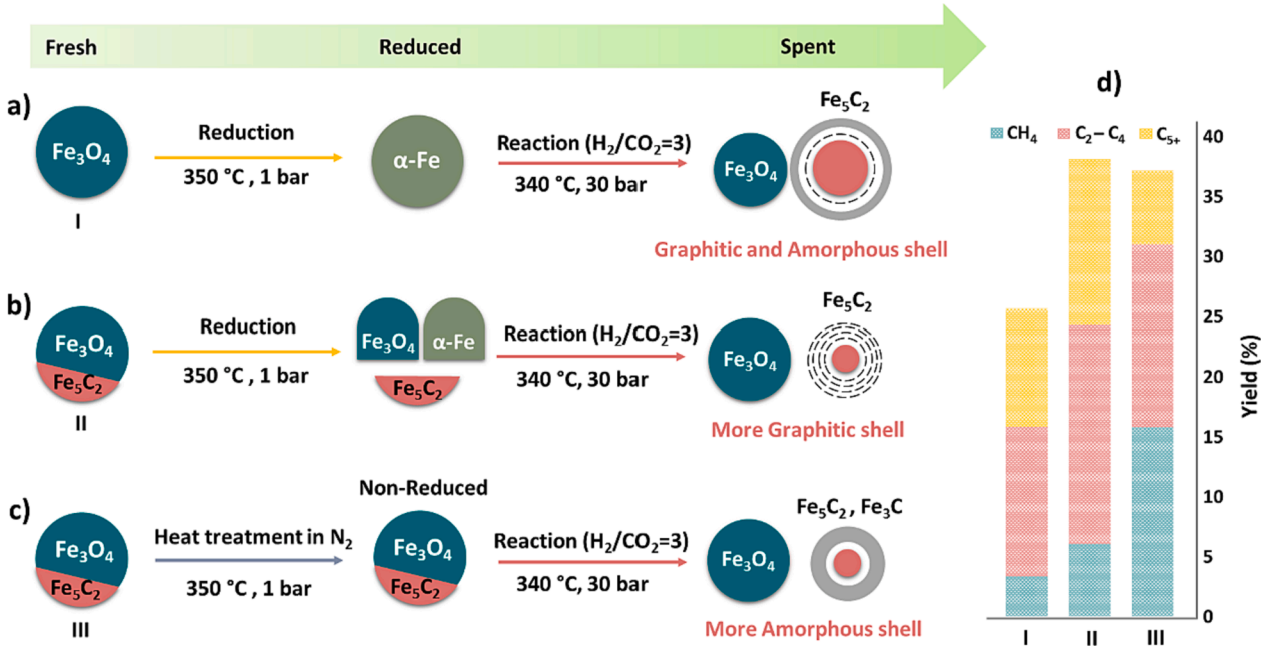

Fig. 11. Scheme proposed for the relationship between structural catalyst properties and performance.

interests or personal relationships that could have appeared to influence the work reported in this paper.

Data availability

Data will be made available on request.

Acknowledgments

A.S. gratefully acknowledges the support of FK 143583, and Z.K. is grateful for the K_21 138714 and SNN_135918 projects from the source of the National Research, Development, and Innovation Fund. The Ministry of Human Capacities through the 20391-3/2018/FEKUSTRAT, as well as Project No. TKP2021-NVA-19 under the TKP2021-NVA funding scheme of the Ministry for Innovation and Technology are acknowledged. Project no. RRF-2.3.1-21-2022-00009, titled National Laboratory for Renewable Energy, has been implemented with the support provided by the Recovery and Resilience Facility of the European Union within the framework of Programme Széchenyi Plan Plus.

Appendix A. Supplementary data

Supplementary data to this article can be found online at https://doi.org/10.1016/j.cej.2024.149787.

References

[1] X. Shang, G. Liu, X. Su, Y. Huang, T. Zhang, A review of the recent progress on direct heterogeneous catalytic CO_2 hydrogenation to gasoline-range hydrocarbons, EES Catal. 1 (2023) 353–368, https://doi.org/10.1039/D3EY00026E.

[2] K.B. Tan, K. Xu, D. Cai, J. Huang, G. Zhan, Rational design of bifunctional catalysts with proper integration manners for CO and CO_2 hydrogenation into value-added products: A review, Chem. Eng. J. 463 (2023) 142262, https://doi.org/10.1016/j.cej.2023.142262.

[3] S. Najari, G. Gróf, S. Saeidi, Enhancement of hydrogenation of CO_2 to hydrocarbons via In-Situ water removal, Int. J. Hydrogen Energy 44 (45) (2019) 24759–24781, https://doi.org/10.1016/j.ijhydene.2019.07.159.

[4] S. Saeidi, S. Najari, G. Gróf, F. Gallucci, Effect of operating conditions and effectiveness factor on hydrogenation of CO_2 to hydrocarbons, Int. J. Hydrogen Energy 44 (54) (2019) 28586–28602, https://doi.org/10.1016/j.ijhydene.2019.08.255.

[5] S. Najari, G. Gróf, S. Saeidi, P. Bihari, W.-H. Chen, Modeling and statistical analysis of the three-side membrane reactor for the optimization of hydrocarbon production from CO_2 hydrogenation, Energ. Conver. Manage. 207 (2020) 112481, https://doi.org/10.1016/j.enconman.2020.112481.

[6] S. Najari, S. Saeidi, G. Gróf, F.J. Keil, A.E. Rodrigues, Kinetic parameters estimation via dragonfly algorithm (DA) and comparison of cylindrical and spherical reactors performance for CO_2 hydrogenation to hydrocarbons, Energy Convers. Manage. 226 (2020) 113550. https://doi.org/10.1016/j.enconman.2020.113550.

[7] S. Saeidi, S. Najari, V. Hessel, K. Wilson, F.J. Keil, P. Concepción, S.L. Suib, A. E. Rodrigues, Recent advances in CO_2 hydrogenation to value-added products — Current challenges and future directions, Prog. Energy Combust. Sci. 85 (2021) 100905, https://doi.org/10.1016/j.pecs.2021.100905.

[8] S. Saeidi, N.A.S. Amin, M.R. Rahimpour, Hydrogenation of CO_2 to value-added products—A review and potential future developments, J. CO_2 Utiliz. 5 (2014) 66–81, https://doi.org/10.1016/j.jcou.2013.12.005.

[9] S. Saeidi, S. Najari, F. Fazlollahi, M.K. Nikoo, F. Sefidkon, J.J. Klemeš, L.L. Baxter, Mechanisms and kinetics of CO_2 hydrogenation to value-added products: A detailed review on current status and future trends, Renew. Sustain. Energy Rev. 80 (2017) 1292–1311, https://doi.org/10.1016/j.rser.2017.05.204.

[10] L. Tang, B.-C. Zhou, X. Liu, S. Xu, J. Wang, W. Xu, X. Liu, L. Chen, A.-H. Lu, Selective synthesis of the core–shell structured catalyst χ-Fe_5C_2 surrounded by nanosized Fe_3O_4 for the conversion of syngas to liquid fuels, Cat. Sci. Technol. (2022), https://doi.org/10.1039/D1CY02241E.

[11] Q. Yang, V.A. Kondratenko, S.A. Petrov, D.E. Doronkin, E. Saraçi, H. Lund, A. Arinchtein, R. Kraehnert, A.S. Skrypnik, A.A. Matvienko, E.V. Kondratenko, Identifying performance descriptors in CO_2 hydrogenation over iron-based catalysts promoted with alkali metals, Angew. Chem. Int. Ed. 61 (22) (2022) e202116517, https://doi.org/10.1002/anie.202116517.

[12] A. Fedorov, H. Lund, V.A. Kondratenko, E.V. Kondratenko, D. Linke, Elucidating reaction pathways occurring in CO_2 hydrogenation over Fe-based catalysts, Appl. Catal. B 328 (2023) 122505, https://doi.org/10.1016/j.apcatb.2023.122505.

[13] M. Iglesias, G.C. de Vries, M. Claeys, G. Schaub, Chemical energy storage in gaseous hydrocarbons via iron Fischer-Tropsch synthesis from H_2/CO_2—Kinetics, selectivity and process considerations, Catal. Today 242 (2015) 184–192, https://doi.org/10.1016/j.cattod.2014.05.020.

[14] A.S. Skrypnik, S.A. Petrov, V.A. Kondratenko, Q. Yang, H. Lund, A.A. Matvienko, E. V. Kondratenko, Descriptors affecting methane selectivity in CO_2 hydrogenation over unpromoted bulk iron(III)-based catalysts, ACS Catal. (2022) 11355–11368, https://doi.org/10.1021/acscatal.2c03375.

[15] E. de Smit, F. Cinquini, A.M. Beale, O.V. Safonova, W. van Beek, P. Sautet, B. M. Weckhuysen, Stability and reactivity of ϵ–χ–θ iron carbide catalyst phases in Fischer–Tropsch synthesis: Controlling μC, J. Am. Chem. Soc. 132 (42) (2010) 14928–14941, https://doi.org/10.1021/ja105853q.

[16] A. Ramirez, S. Ould-Chikh, L. Gevers, A.D. Chowdhury, E. Abou-Hamad, A. Aguilar-Tapia, J.-L. Hazemann, N. Wehbe, A.J. Al Abdulghani, S.M. Kozlov, L. Cavallo, J. Gascon, Tandem conversion of CO_2 to valuable hydrocarbons in highly concentrated potassium iron catalysts, ChemCatChem 11(12) (2019) 2879-2886. https://doi.org/10.1002/cctc.201900762.

[17] A.S. Skrypnik, H. Lund, Q. Yang, E.V. Kondratenko, Spatial analysis of CO2 hydrogenation to higher hydrocarbons over alkali-metal promoted iron(ii)oxalate-derived catalysts, Cat. Sci. Technol. (2023), https://doi.org/10.1039/D3CY00143A.

[18] J. Wei, Q. Ge, R. Yao, Z. Wen, C. Fang, L. Guo, H. Xu, J. Sun, Directly converting CO_2 into a gasoline fuel, Nat. Commun. 8 (1) (2017) 15174, https://doi.org/10.1038/ncomms15174.

[19] Y. Li, L. Zeng, G. Pang, X. Wei, M. Wang, K. Cheng, J. Kang, J.M. Serra, Q. Zhang, Y. Wang, Direct conversion of carbon dioxide into liquid fuels and chemicals by coupling green hydrogen at high temperature, Appl. Catal. B 324 (2023) 122299, https://doi.org/10.1016/j.apcatb.2022.122299.

[20] Q. Zhao, X. Xu, G. Fan, F. Li, Crucial role of surface FeO_x components on supported Fe-based nanocatalysts for CO_2 hydrogenation to light olefins, Ind. Eng. Chem. Res. 62 (24) (2023) 9420–9432, https://doi.org/10.1021/acs.iecr.3c00500.

[21] M. Amoyal, R. Vidruk-Nehemya, M.V. Landau, M. Herskowitz, Effect of potassium on the active phases of Fe catalysts for carbon dioxide conversion to liquid fuels through hydrogenation, J. Catal. 348 (2017) 29–39, https://doi.org/10.1016/j.jcat.2017.01.020.

[22] D. Weber, N. Rui, F. Zhang, H. Zhang, D. Vovchok, M. Wildy, K. Arizapana, A. Saporita, J.Z. Zhang, S.D. Senanayake, P. Lu, C. Zhang, Carbon nanosphere-encapsulated Fe core-shell structures for catalytic CO_2 hydrogenation, ACS Applied Nano Materials 5 (8) (2022) 11605–11616, https://doi.org/10.1021/acsanm.2c02602.

[23] S. Das, J. Pérez-Ramírez, J. Gong, N. Dewangan, K. Hidajat, B.C. Gates, S. Kawi, Core–shell structured catalysts for thermocatalytic, photocatalytic, and electrocatalytic conversion of CO_2, Chem. Soc. Rev. 49 (10) (2020) 2937–3004, https://doi.org/10.1039/C9CS00713J.

[24] A.Y. Khodakov, W. Chu, P. Fongarland, Advances in the development of novel cobalt Fischer–Tropsch catalysts for synthesis of long-chain hydrocarbons and clean fuels, Chem. Rev. 107 (5) (2007) 1692–1744, https://doi.org/10.1021/cr050972v.

[25] Y. Gao, L. Shao, S. Yang, J. Hu, S. Zhao, J. Dang, W. Wang, X. Yan, P. Yang, Recent advances in iron-based catalysts for Fischer-Tropsch to olefins reaction, Catal. Commun. 181 (2023) 106720, https://doi.org/10.1016/j.catcom.2023.106720.

[26] W. Malik, J.P. Victoria Tafoya, S. Doszczeczko, A.B. Jorge Sobrido, V.K. Skoulou, A.N. Boa, Q. Zhang, T. Ramirez Reina, R. Volpe, Synthesis of a graphene-encapsulated Fe_3C/Fe catalyst supported on sporopollenin exine capsules and its use for the reverse water-gas shift reaction, ACS Sustain. Chem. Eng. (2023), https://doi.org/10.1021/acssuschemeng.3c00495.

[27] Z. Fu, D. Luo, L. Chen, Y. Wei, M. Ren, W. Wang, C. Zhang, S. Sun, Carbon defects promoting syngas into liquid fuels over Fe_3C@C catalysts, Cat. Sci. Technol. 13 (7) (2023) 2010–2014, https://doi.org/10.1039/D3CY00213F.

[28] S. De, A. Dokania, A. Ramirez, J. Gascon, Advances in the design of heterogeneous catalysts and thermocatalytic processes for CO_2 utilization, ACS Catal. 10 (23) (2020) 14147–14185, https://doi.org/10.1021/acscatal.0c04273.

[29] Q. Chang, C. Zhang, C. Liu, Y. Wei, A.V. Cheruvathur, A.I. Dugulan, J. W. Niemantsverdriet, X. Liu, Y. He, M. Qing, L. Zheng, Y. Yun, Y. Yang, Y. Li, Relationship between iron carbide phases (ε-Fe_2C, Fe_7C_3, and χ-Fe_5C_2) and catalytic performances of Fe/SiO_2 Fischer-Tropsch catalysts, ACS Catal. 8 (4) (2018) 3304–3316, https://doi.org/10.1021/acscatal.7b04085.

[30] J. Huang, S. Jiang, M. Wang, X. Wang, J. Gao, C. Song, Dynamic evolution of Fe and carbon species over different ZrO_2 supports during CO prereduction and their effects on CO_2 hydrogenation to light olefins, ACS Sustain. Chem. Eng. 9 (23) (2021) 7891–7903, https://doi.org/10.1021/acssuschemeng.1c01777.

[31] Y. Chen, J. Wei, M.S. Duyar, V.V. Ordomsky, A.Y. Khodakov, J. Liu, Carbon-based catalysts for Fischer-Tropsch synthesis, Chem. Soc. Rev. 50 (4) (2021) 2337–2366, https://doi.org/10.1039/D0CS00905A.

[32] X. Yang, H. Zhang, Y. Liu, W. Ning, W. Han, H. Liu, C. Huo, Preparation of iron carbides formed by iron oxalate carburization for Fischer-Tropsch synthesis, Catalysts 9 (4) (2019) 347, https://doi.org/10.3390/catal9040347.

[33] L. Tang, L. He, Y. Wang, B. Chen, W. Xu, X. Duan, A.-H. Lu, Selective fabrication of χ-Fe_5C_2 by interfering surface reactions as a highly efficient and stable Fischer-Tropsch synthesis catalyst, Appl. Catal. B 284 (2021) 119753, https://doi.org/10.1016/j.apcatb.2020.119753.

[34] A.S. Skrypnik, Q. Yang, A.A. Matvienko, V.Y. Bychkov, Y.P. Tulenin, H. Lund, S. A. Petrov, R. Kraehnert, A. Arinchtein, J. Weiss, A. Brueckner, E.V. Kondratenko, Understanding reaction-induced restructuring of well-defined $Fe_xO_yC_z$ compositions and its effect on CO_2 hydrogenation, Appl. Catal. B 291 (2021) 120121, https://doi.org/10.1016/j.apcatb.2021.120121.

[35] A.S. Skrypnik, S.A. Petrov, V.A. Kondratenko, Q. Yang, A.A. Matvienko, E. V. Kondratenko, Spatially resolved analysis of CO_2 hydrogenation to higher hydrocarbons over alkali-metal promoted well-defined $Fe_xO_yC_z$, J. Catal. (2023), https://doi.org/10.1016/j.jcat.2023.06.019.

[36] S. Lyu, L. Wang, Z. Li, S. Yin, J. Chen, Y. Zhang, J. Li, Y. Wang, Stabilization of ε-iron carbide as high-temperature catalyst under realistic Fischer-Tropsch

synthesis conditions, Nat. Commun. 11 (1) (2020) 6219, https://doi.org/10.1038/s41467-020-20068-5.
[37] J.H. Lee, H.-K. Lee, D.H. Chun, H. Choi, G.B. Rhim, M.H. Youn, H. Jeong, S. W. Kang, J.-I. Yang, H. Jung, C.S. Kim, J.C. Park, Phase-controlled synthesis of thermally stable nitrogen-doped carbon supported iron catalysts for highly efficient Fischer-Tropsch synthesis, Nano Res. 12 (10) (2019) 2568–2575, https://doi.org/10.1007/s12274-019-2487-4.
[38] S.O. Moussa, L.S. Panchakarla, M.Q. Ho, M.S. El-Shall, Graphene-supported, iron-based nanoparticles for catalytic production of liquid hydrocarbons from synthesis gas: the role of the graphene support in comparison with carbon nanotubes, ACS Catal. 4 (2) (2014) 535–545, https://doi.org/10.1021/cs4010198.
[39] M.A. Nawaz, M. Saif, M. Li, G. Song, W. Zihao, C. Chen, D. Liu, Elucidating the synergistic fabrication of dual embedded (χ-Fe_5C_2 + θ-Fe_3C) carbide nanocomposites in Na FeCa@AC/HZSM-5 integrated catalyst for syngas conversion to aromatics, Fuel 324 (2022) 124390, https://doi.org/10.1016/j.fuel.2022.124390.
[40] K. Jin, C. Wen, L. Chen, Q. Jiang, X. Zhuang, X. Xu, H. Wang, L. Ma, C. Wang, Q. Zhang, In situ synthesis of highly dispersed Fe/C catalysts with pomelo peel as carbon source in CO_2 hydrogenation to light olefins, Fuel 333 (2023) 126412, https://doi.org/10.1016/j.fuel.2022.126412.
[41] B.-Y. Chen, G. Dobele, A. Plavniece, A. Volperts, L. Tamasauskaite-Tamasiunaite, E. Norkus, C.-L. Chen, Y.-C. Lin, Catalytic hydrogenation of CO_2 to light olefins by using K-doped FeC_x catalysts derived from the Fe-chitosan complex, Int. J. Hydrogen Energy 48 (11) (2023) 4276–4286, https://doi.org/10.1016/j.ijhydene.2022.11.010.
[42] J. Liu, G. Zhang, X. Jiang, J. Wang, C. Song, X. Guo, Insight into the role of Fe_5C_2 in CO_2 catalytic hydrogenation to hydrocarbons, Catal. Today 371 (2021) 162–170, https://doi.org/10.1016/j.cattod.2020.07.032.
[43] J. Liu, A. Zhang, X. Jiang, M. Liu, J. Zhu, C. Song, X. Guo, Direct transformation of carbon dioxide to value-added hydrocarbons by physical mixtures of Fe_5C_2 and K-modified Al_2O_3, Ind. Eng. Chem. Res. 57 (28) (2018) 9120–9126, https://doi.org/10.1021/acs.iecr.8b02017.
[44] C. Wen, J. Jiang, C. Chiliu, Z. Tian, X. Xu, J. Wu, C. Wang, L. Ma, Single-step selective conversion of carbon dioxide to aromatics over Na-Fe_3O_4/hierarchical HZSM-5 zeolite catalyst, Energy Fuel 34 (9) (2020) 11282–11289, https://doi.org/10.1021/acs.energyfuels.0c02120.
[45] J. Zhang, M. Abbas, W. Zhao, J. Chen, Enhanced stability of a fused iron catalyst under realistic Fischer-Tropsch synthesis conditions: insights into the role of iron phases (χ-Fe_5C_2, θ-Fe_3C and α-Fe), Cat. Sci. Technol. 12 (13) (2022) 4217–4227, https://doi.org/10.1039/D2CY00703G.
[46] Y. Zhang, D. Fu, X. Liu, Z. Zhang, C. Zhang, B. Shi, J. Xu, Y.-F. Han, Operando Spectroscopic Study of Dynamic Structure of Iron Oxide Catalysts during CO_2 Hydrogenation, Chem., Mater. Sci. 10 (6) (2018) 1272–1276, https://doi.org/10.1002/cctc.201701779.
[47] J. Zhu, P. Wang, X. Zhang, G. Zhang, R. Li, W. Li, T.P. Senftle, W. Liu, J. Wang, Y. Wang, A. Zhang, Q. Fu, C. Song, X. Guo, Dynamic structural evolution of iron catalysts involving competitive oxidation and carburization during CO_2 hydrogenation, 8(5) (2022) eabm3629. https://doi.org/doi:10.1126/sciadv.abm3629.
[48] X. Liu, C. Zhang, P. Tian, M. Xu, C. Cao, Z. Yang, M. Zhu, J. Xu, Revealing the effect of sodium on iron-based catalysts for CO_2 hydrogenation: insights from calculation and experiment, J. Phys. Chem. C 125 (14) (2021) 7637–7646, https://doi.org/10.1021/acs.jpcc.0c11123.
[49] Y. Fu, C.C. Amoo, H. Qi, H. Liu, L. Zhu, P. Lu, R. Yang, C. Xing, S. Wang, J. Sun, EDTA chemical directly orient CO_2 hydrogenation towards olefins, Chem. Eng. J. 438 (2022) 135597, https://doi.org/10.1016/j.cej.2022.135597.
[50] C.C. Amoo, J.I. Orege, Q. Ge, J. Sun, Exploiting the latency of carbon as catalyst in CO_2 hydrogenation, Chem. Eng. J. 471 (2023) 144606, https://doi.org/10.1016/j.cej.2023.144606.
[51] R. He, Y. Wang, M. Li, J. Liu, Y. Gu, W. Wang, Q. Liu, N. Tsubaki, M. Wu, Tailoring the CO_2 hydrogenation performance of Fe-based catalyst via unique confinement effect of the carbon shell, Chem. A Eur. J. 29 (65) (2023) e202301918, https://doi.org/10.1002/chem.202301918.
[52] T. Yamashita, P. Hayes, Analysis of XPS spectra of Fe^{2+} and Fe^{3+} ions in oxide materials, Appl. Surf. Sci. 254 (8) (2008) 2441–2449, https://doi.org/10.1016/j.apsusc.2007.09.063.
[53] J. Chen, S.J. Han, H.-G. Park, K. Nasriddinov, C. Zhang, K.-W. Jun, S.K. Kim, Benchmarking promoters of Fe/activated carbon catalyst for stable hydrogenation of CO_2 to liquid hydrocarbons, Appl. Catal. B 325 (2023) 122370, https://doi.org/10.1016/j.apcatb.2023.122370.
[54] A. Arinchtein, M.-Y. Ye, Q. Yang, C. Kreyenschulte, A. Wagner, M. Frisch, A. Brückner, E. Kondratenko, R. Kraehnert, Dynamics of reaction-induced changes of model-type iron oxide phases in the CO_2-Fischer-Tropsch-synthesis, ChemCatChem 14 (14) (2022) e202200240, https://doi.org/10.1002/cctc.202200240.
[55] Q. Yang, V.A. Kondratenko, A.S. Skrypnik, H. Lund, S. Bartling, J. Weiss, A. Brückner, E.V. Kondratenko, Understanding of the fate of α-Fe_2O_3 in CO_2 hydrogenation through combined time-resolved in situ characterization and microkinetic analysis, ACS Catal. 13 (13) (2023) 9064–9077, https://doi.org/10.1021/acscatal.3c01340.
[56] G. Srinivas, Y. Zhu, R. Piner, N. Skipper, M. Ellerby, R. Ruoff, Synthesis of graphene-like nanosheets and their hydrogen adsorption capacity, Carbon 48 (3) (2010) 630–635, https://doi.org/10.1016/j.carbon.2009.10.003.
[57] X. Li, Y. Chen, P. Wu, M.U. Nisa, Z. Li, Core-shell Co@C catalyst: effect of a confined carbon microenvironment on syngas conversion, Ind. Eng. Chem. Res. 59 (33) (2020) 14636–14642, https://doi.org/10.1021/acs.iecr.0c01411.
[58] Q. Yang, E.A. Fedorova, S.A. Petrov, J. Weiss, H. Lund, A.S. Skrypnik, C. R. Kreyenschulte, V.Y. Bychkov, A.A. Matvienko, A. Brueckner, E.V. Kondratenko, Activity and selectivity descriptors for iron carbides in CO_2 hydrogenation, Appl. Catal. B 327 (2023) 122450, https://doi.org/10.1016/j.apcatb.2023.122450.
[59] D. Fu, W. Dai, X. Xu, W. Mao, J. Su, Z. Zhang, B. Shi, J. Smith, P. Li, J. Xu, Y.-F. Han, Probing The structure evolution of iron-based Fischer-Tropsch to produce olefins by operando Raman spectroscopy, ChemCatChem 7 (5) (2015) 752–756, https://doi.org/10.1002/cctc.201402980.
[60] M.K. Khan, P. Butolia, H. Jo, M. Irshad, D. Han, K.-W. Nam, J. Kim, Selective conversion of carbon dioxide into liquid hydrocarbons and long-chain α-olefins over Fe-amorphous AlO_x bifunctional catalysts, ACS Catal. 10 (18) (2020) 10325–10338, https://doi.org/10.1021/acscatal.0c02611.
[61] H. Wang, X. Nie, Y. Liu, M.J. Janik, X. Han, Y. Deng, W. Hu, C. Song, X. Guo, Mechanistic insight into hydrocarbon synthesis via CO_2 hydrogenation on χ-Fe_5C_2 catalysts, ACS Appl. Mater. Interfaces 14 (33) (2022) 37637–37651, https://doi.org/10.1021/acsami.2c07029.
[62] Q. Jiang, G. Song, Y. Zhai, C. Chen, Z. Wang, H. Yuan, Z. Zhang, D. Liu, Selective hydrogenation of CO_2 to aromatics over composite catalyst comprising NaZnFe and polyethylene glycol-modified HZSM-5 with intra- and intercrystalline mesoporous structure, Ind. Eng. Chem. Res. 62 (23) (2023) 9188–9200, https://doi.org/10.1021/acs.iecr.3c00915.
[63] J.I. Orege, J. Wei, Y. Han, M. Yang, X. Sun, J. Zhang, C.C. Amoo, Q. Ge, J. Sun, Highly stable Sr and Na co-decorated Fe catalyst for high-valued olefin synthesis from CO_2 hydrogenation, Appl. Catal. B 316 (2022) 121640, https://doi.org/10.1016/j.apcatb.2022.121640.
[64] D. Ye, W. Tang, T. Zhang, L. Lv, Z. Zou, R.K. Gupta, S. Tang, Enhancing the synergism of Fe_3O_4 and Fe_5C_2 to improve the process of CO_2 hydrogenation to olefines, Colloids Surf., A Physicochem. Eng. Asp. 654 (2022) 130145, https://doi.org/10.1016/j.colsurfa.2022.130145.
[65] H. Zhao, J.-X. Liu, C. Yang, S. Yao, H.-Y. Su, Z. Gao, M. Dong, J. Wang, I. Rykov Alexandre, J. Wang, Y. Hou, W.-X. Li, D. Ma, Synthesis of iron-carbide nanoparticles: identification of the active phase and mechanism of Fe-based Fischer–Tropsch synthesis, CCS Chem. 3(11) (2020) 2712-2724. https://doi.org/10.31635/ccschem.020.202000555.
[66] V.V. Ordomsky, B. Legras, K. Cheng, S. Paul, A.Y. Khodakov, The role of carbon atoms of supported iron carbides in Fischer-Tropsch synthesis, Cat. Sci. Technol. 5 (3) (2015) 1433–1437, https://doi.org/10.1039/C4CY01631A.
[67] M. Claeys, E. van Steen, T. Botha, R. Crous, A. Ferreira, A. Harilal, D.J. Moodley, P. Moodley, E. du Plessis, J.L. Visagie, Oxidation of Hägg carbide during high-temperature Fischer-Tropsch synthesis: size-dependent thermodynamics and in situ observations, ACS Catal. 11 (22) (2021) 13866–13879, https://doi.org/10.1021/acscatal.1c03719.
[68] S. Li, G.D. Meitzner, E. Iglesia, Structure and site evolution of iron oxide catalyst precursors during the Fischer–Tropsch synthesis, J. Phys. Chem. B 105 (24) (2001) 5743–5750, https://doi.org/10.1021/jp010288u.